

1 Orbitally forced environmental changes during the accumulation 2 of a Pliensbachian (Lower Jurassic) black shale in northern Iberia

3 Naroa Martínez-Braceras^{1,2}; Aitor Payros¹; Jaume Dinarès-Turell³; Idoia Rosales⁴; Javier
4 Arostegi¹ and Roi Silva-Casal⁵

5 ¹ Department of Geology, Faculty of Science and Technology, University of the Basque
6 Country (UPV/EHU), P.O. Box 644, 48080 Bilbao, Spain

7 ² Laboratorio de Evolución Humana, Departamento de Historia, Geografía y
8 Comunicación, Universidad de Burgos, Edificio I+D+I, Plaza de Misael Bañuelos/n,
9 09001 Burgos, Spain

10 ³ Istituto Nazionale di Geofisica e Vulcanologia, Via di Vigna Murata 605, 00142 Rome,
11 Italy

12 ⁴ Centro Nacional Instituto Geológico y Minero de España (IGME, CSIC), La Calera 1,
13 Tres Cantos, 28760 Madrid, Spain

14 ⁵ Dpto. Dinàmica de la Terra i de l'Oceà, Facultat de Ciències de la Terra, ~~UB~~ [Universitat](#)
15 [de Barcelona](#), 08028 Barcelona, [Spain](#).

16 Correspondence to: Naroa Martínez Braceras (naroa.martinez@ehu.es)

17 Abstract

18 Lower Pliensbachian hemipelagic successions from the north Iberian palaeomargin are
19 characterized by the occurrence of organic-rich calcareous rhythmites of decimetre-thick
20 limestone and marl beds and thicker black shale intervals. Understanding the genetic
21 mechanisms of the cyclic lithologies and ~~involved processes involved~~ along with the
22 nature of the carbon cycle is of primary interest. ~~The This~~ cyclostratigraphic study, carried
23 out in one of the black ~~shale intervals~~ exposed in Santiurde de Reinosa (Basque-
24 Cantabrian Basin), ~~revealed reveals~~ that the calcareous rhythmites responded to periodic
25 environmental variations in the Milankovitch-cycle band, ~~with the prevalence of and were~~
26 ~~likely driven by eccentricity-modulated precession precession, short eccentricity and long~~
27 ~~eccentricity cycles.~~

28 The main environmental processes that determined the formation of the rhythmite were
29 deduced on the basis of the integrated sedimentological, mineralogical and geochemical
30 study of an eccentricity bundle. The formation of precession couplets was controlled by
31 variations in carbonate production and dilution by terrigenous supplies, along with
32 periodic changes in bottom water oxygenation. Precessional configurations with marked
33 annual seasonality, increased terrigenous input (by rivers or wind) to marine areas and
34 boosted organic productivity in surface ~~waterswater~~. The great accumulation of organic
35 matter on the seabed eventually decreased bottom ~~waterswater~~ oxygenation, which might
36 also be influenced by reduced ocean ventilation. Thus, deposition of organic-rich marls
37 and shales occurred when annual seasonality was ~~maximummaxima~~. On the contrary, a

38 reduction in terrestrial inputs at precessional configurations with minimal seasonality
39 ~~diminished~~ shallow organic productivity, ~~which~~, added to an intensification of vertical
40 ~~seawater~~-mixing, contributed to increasing the oxidation of organic matter. These
41 conditions also favoured greater production and basinward ~~exportation~~ of carbonate mud
42 in shallow marine areas, causing the formation of limy hemipelagic beds. Short
43 eccentricity cycles modulated the amplitude of precession driven variations in terrigenous
44 input and oxygenation of bottom ~~seawaters~~water. Thus, the amplitude of the contrast
45 between successive precessional beds increased when the Earth's orbit was elliptical and
46 diminished when it was circular. The data also suggest that short eccentricity cycles
47 affected short-term sea level changes, probably through ~~orbitally~~ modulated aquifer-
48 eustasy.

49 1. Introduction

50 As a consequence of the gravitational interaction between astronomical bodies, the
51 Earth's axial orientation and orbit vary cyclically at timescales that range from tens of
52 thousands to ~~a few~~ million years (Berger and Loutre, 1994). These variations in orbital
53 configuration regulate the latitudinal ~~and temporal~~ distribution of solar radiation
54 (insolation), which determines the contrast between seasons. ~~These periodic changes in~~
55 ~~the climatic system can affect the evolution of a wide range of sedimentary environments,~~
56 ~~from terrestrial to deep marine (Einsele and Ricken, 1991). These periodic changes in the~~
57 ~~climatic system can be recorded as cyclic stratigraphic successions, the so-called~~
58 ~~rhythmites, in a wide range of sedimentary environments (Einsele and Ricken, 1991).~~ As
59 the open ocean is hardly affected by processes that may ~~erode the seabed or~~ interrupt the
60 continuous settling of fine-grained particles ~~or erode the seabed~~, deep marine pelagic ~~and~~
61 ~~hemipelagic~~ sediments accumulate at a generally constant, but slow, ~~rate~~ (few cm/ky),
62 ~~sedimentation rate~~. Thus, pelagic ~~and hemipelagic~~ ~~rhythmites successions~~ from both
63 ~~oceanic sediment cores and outcrops~~ ~~indurate successions~~ contain accurate records of
64 orbitally modulated, quasi-periodic climate-change episodes, ~~which provide high~~
65 ~~resolution astrochronologies~~ (Hinnov, 2013). ~~These periodic changes in the climatic~~
66 ~~system are generally recorded as cyclic stratigraphic successions, the so-called~~
67 ~~rhythmites, in both pelagic and hemipelagic successions (Einsele and Ricken, 1991).~~

68 Significant progress in Early Jurassic cyclostratigraphy has been made in the last few
69 decades thanks to the study of exceptional orbitally modulated sedimentary records
70 obtained from deep marine environments of the ~~Perytethyan-peri-Tethyan~~ realm (e.g.,
71 Cardigan and Cleveland Basins by Hüsing et al., 2014, Storm et al., 2020; Pieńkowski et
72 al., 2021; Paris Basin by Charbonnier et al., 2023). Although these studies provided
73 relevant astrochronological information, they did not focus on the climatic and
74 environmental impact of the orbital cycles ~~on the sedimentary record~~. Other studies
75 deduced a control of long-term orbital cycles on the Jurassic carbon cycle (Martinez and
76 Dera, 2015; Ikeda et al., 2016; Hollar et al 2021; Zhang et al., 2023), but the climatic and
77 environmental influence of short-term cycles has been less studied (Hinnov and Park,
78 1999; Ikeda et al., 2016; Hollar et al., 2023).

79 The aim of this study ~~was is~~ to analyze the climatic and environmental impact of short-
80 term ~~astronomical-orbital~~ cycles on Lower Jurassic deep marine deposits. To this end, a
81 hemipelagic alternation of limy and marl/shale beds was analyzed in the Santiurde de
82 Reinosa section (hereafter referred to as the Santiurde section), Basque-Cantabrian Basin
83 (BCB), Cantabria province, Spain. In order to determine if sedimentation was orbitally
84 forced, a cyclostratigraphic analysis of the hemipelagic ~~rhythmites~~ was ~~firstly~~ undertaken.
85 Subsequently, an integrated multiproxy study was performed in a selected interval of the
86 section in order to disentangle what ~~sedimentary processes and~~ environmental factors
87 influenced ~~on~~ the formation of the hemipelagic ~~rhythmites~~.

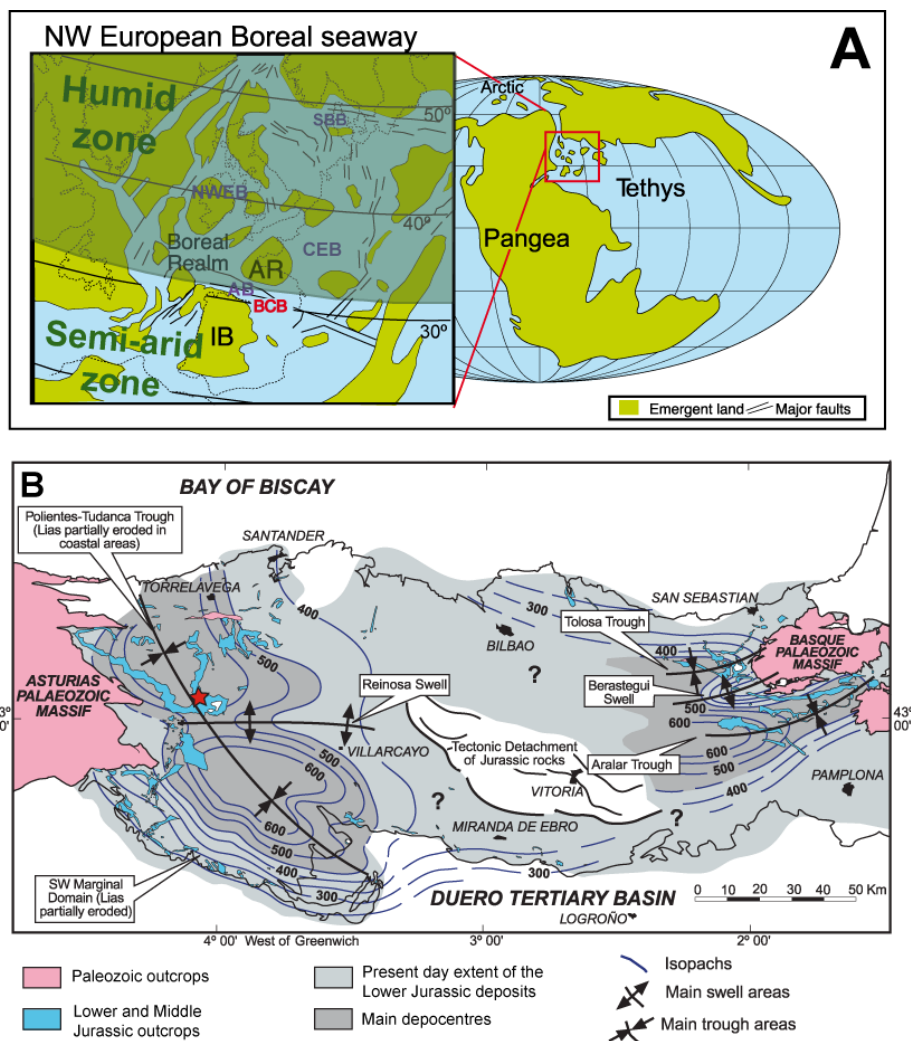
88 -2. Geological setting

89 In ~~E~~arly Jurassic times the BCB was located to the south of ~~the Armorican massif~~ and
90 to the north of the Iberian Massif, ~~being part of within~~ the Laurasian epicontinental seaway
91 ~~which that connected the Boreal Sea with the northwestern Tethyan Ocean connected the~~
92 ~~Boreal Sea with the southern Tethyan Ocean~~ (Fig. 1A; Aurell et al., 2002; Rosales et al.,
93 2004). Previous palaeogeographic reconstructions located the north Iberian margin at
94 approximately 30°N palaeolatitude (Quesada et al., 2005; Osete et al., 2010). Hence, the
95 ~~emerged Iberian~~ source area was located in the semiarid belt but close to the boundary
96 with the humid climatic zone (temperate climate characterized by megamonsoons; Dera
97 et al., 2009; Deconinck et al., 2020), which made it especially sensitive to astronomically
98 driven climate change. ~~Such periodic climate change episodes alternately increased and~~
99 ~~decreased the influence of one or the other climatic belts (Martinez and Dera, 2015).~~

100 Hettangian and lower Sinemurian deposits accumulated in evaporitic tidal flats and
101 shallow carbonate ramps, whereas the overlying Sinemurian-Callovian succession ~~was~~
102 accumulated ~~in an open marine, outer ramp environment, which was generally in deep~~
103 ~~and quiet conditions below storm wave base in relatively deep, open marine conditions~~
104 (Aurell et al., 2002; Quesada et al., 2005). ~~Hemipelagic sedimentation (sensu Henrich and~~
105 ~~Hüneke, 2011) prevailed in the outer ramp, as autochthonous pelagic production was~~
106 ~~mixed with periplatform carbonate advection and siliciclastic input from the southern~~
107 ~~continental margin.~~ Differential subsidence during the Jurassic related to early
108 mobilization of underlying Triassic salt resulted in the creation of several troughs in the
109 BCB (Fig. 1B, Quesada et al., 2005).

110 Pliensbachian ~~(192.9–184.2 Ma)~~ hemipelagic successions of the BCB (Camino
111 Formation; Quesada et al., 2005) are characterized by the occurrence of three black shale
112 ~~(BS)~~ intervals ~~(BSIs)~~, each several tens of metres thick (Braga et al., 1988; Quesada et
113 al., 1997, 2005; Quesada and Robles 2012; Rosales et al., 2001, 2004, 2006). ~~These three~~
114 ~~BSIs are composed of alternating black shale layers and limestone/marly limestone beds,~~
115 ~~and are separated from each other by decametric intervals devoid of black shale layers, in~~
116 ~~which only hemipelagic marls, marly limestones and limestones occur.~~ ~~These three BS~~
117 ~~intervalBSIs~~ can be correlated with similar coeval deposits in neighbouring basins in
118 Asturias (Borrego et al., 1996; Armendáriz et al., 2012; Bádenas et al., 2012, 2013;
119 Gómez et al., 2016). Coeval organic rich marine facies have also been observed in other

120 Thetyan lower Jurassic successions from Portugal (Silva et al., 2011), the United
 121 Kingdom (Hüsing et al., 2014), France (Bougeault et al., 2017) and Germany (Pieńkowski
 122 et al., 2008). The BCB Pliensbachian BS intervalBSIs present relatively high organic
 123 carbon content (2–6wt%), high pyrite concentrations and scarce benthic faunas. Thermal
 124 maturity analysis showed that the BS intervalBSIs found at the depocentres are
 125 overmature today, but they sourced the only oil reservoir discovered in inland Iberia
 126 (Quesada et al., 1997, 2005; Quesada and Robles, 2012; Permanyer et al., 2013).
 127 Pyrolysis of thermally immature samples from marginal areas showed total organic
 128 carbon values of up to 20 wt% and hydrogen index values up to 600-750 mg HC/g TOC
 129 (Suárez-Ruiz and Prado, 1987; Quesada et al., 1997). Analyses on of organic matter (OM)
 130 showed that the assemblage is mainly composed of marine type-II kerogens, in which
 131 amorphous and algal material prevail (Quesada et al., 1997, 2005; Permanyer et al., 2013).
 132 More specifically, the analysis revealed a low content in gammaceranes, which suggests
 133 normal salinity conditions, and great abundance of triclinc triterpanes, which can be
 134 associated to *Tasmanites* type unicellular green algae with organic theca. In addition, the
 135 high content in isorenieratene byproducts, such as aryl-isoprenoids, indicates the
 136 occurrence of photosynthetic and sulfurous green algae communities (*Chlorobiaceae*)
 137 developed in oxygen-depleted conditions.



139 Figure 1. A) Palaeogeography and climatic zonation (modified from Quesada et al., 2005; Dera et al., 2009; Ostete et
140 al., 2010) of Western Europe in Early Jurassic times. IB: Iberian massif, AR: Armorican massif, AB: Asturian Basin,
141 BCB: Basque-Cantabrian Basin, CEB: Central European Basin, NWEB: NW European Basin, SBB: South Boreal
142 Basin. B) Simplified geographic and geological map of Lower and Middle Jurassic outcrops in the BCB area, with
143 location of the studied Santiurde section (red star). Superimposed isopach map shows the thickness of the Lower
144 Jurassic rocks and the basin configuration in sedimentary troughs and swells (modified from Quesada et al., 2005).

145 The Santiurde section studied herein is exposed at exit 144 of motorway A67 (UTM
146 X411431.091 Y4769002.593; Fig. 1B), approximately 50 km south-west of Santander
147 and 1 km north-west of a coeval section studied by others at the train station in the same
148 locality (e.g., Rosales et al., 2001, 2004, 2006; Quesada et al., 2005; Fig. S1) ~~with which
149 a bed-by-bed correlation can be readily carried out.~~ The studied succession begins with
150 2.5 m of alternating grey limestones and thin marlstones (Puerto Pozazal Formation),
151 ~~which are overlain followed~~ by 20 m of the lower part of the Pliensbachian Camino
152 Formation, ~~which are~~ mainly made up of alternations of hemipelagic marls, limestones
153 and overmature black shales (Rosales et al., 2004; Quesada et al., 2005). ~~Thus, the studied
154 section includes the oldest BSI of the Camino Formation (BSI-1 in Fig. 2A), which
155 according to regional biostratigraphy corresponds to the older part of the Early
156 Pliensbachian-Uptonia jamesoni ammonite Zone (Braga et al., 1988) and to the latter part
157 of calcareous nannofossil Zone NJ3 (Fraguas et al., 2015). The section includes the oldest
158 (Uptonia jamesoni Zone) of the BS intervals identified in the Camino Formation (Fig.
159 2A).~~

160 -3. Materials and methods

161 3.1. Cyclostratigraphic analysis of the Santiurde section

162 A detailed cm-scale stratigraphic log was measured in a 30.4022.5 m thick succession
163 that exposes the transition from the Puerto Pozazal Formation to the Pliensbachian
164 Camino Formation. A broad range of sedimentological features, such as bed shape,
165 thickness, composition, palaeontological content and structures, were annotated. A total
166 of 373 hand samples were collected, with a resolution of at least 3 samples per bed,
167 avoiding visible skeletal components, burrows and veins. The ~~weight-mass-normalized~~
168 low-field magnetic susceptibility (MS) of the samples was measured using a Kappabridge
169 KLY-3 instrument (Geophysika Brno) housed at the Geology department of the
170 University of the Basque Country, Bilbao, Spain. Subsequently, rock-powder samples
171 were obtained and stored in transparent antiglare prismatic vials, which were scanned in
172 a dark room using a desktop office scanner. The average colour (RGB value) of the
173 scanned images of rock-powder samples was determined using the ImageJ software and
174 following the protocol in Dinarès-Turell et al. (2018) and Martínez-Braceras et al. (2023).

175 In order to carry out a cyclostratigraphic analysis, the Acycle software (Li et al., 2019)
176 and the Astrochron package for R (Meyers et al., 2014) were used. The MS and colour
177 data series were linearly interpolated and detrended first. Subsequently, power spectra
178 were obtained using the 2π -Multi Taper Method (MTM) with three tapers, and confidence
179 levels (CL) were calculated following robust red-noise modelling (Mann and Lees 1996).
180 In addition, Evolutive Harmonic Analysis (EHA; Meyers et al., 2001) and Wavelet
181 analyses (Torrence and Compo, 1998) were also carried out in order to examine the

182 variability of the main frequency bands throughout the succession. Finally, the most
183 significant frequency bands identified in the data series were isolated by Gaussian
184 bandpass filtering.

185 3.2. Multiproxy analysis of Bundle 9

186 An integrated analysis of several environmentally sensitive proxies was undertaken in the
187 19 beds found between ~~20-3012.4~~ and ~~23-85-15.95~~ m of the stratigraphic succession. This
188 interval includes a complete eccentricity bundle (B9, see results below), as well as the
189 uppermost and lowermost ~~beds-couplets~~ of the underlying and overlying bundles,
190 respectively. Fifty-seven samples, ~~with a resolution of 3 samples per bed (21 shales, 9~~
191 ~~marls, 12 marly limestones and 15 limestones)~~, were collected in order to perform a
192 calcimetric analysis by measuring the carbonate percentage in 1 g of powder of each
193 sample using a FOGL digital calcimeter (BD inventions; accuracy of 0.5%) housed at the
194 University of the Basque Country. These samples were also analysed for inorganic
195 $\delta^{13}\text{C}_{\text{carb}}$ and $\delta^{18}\text{O}_{\text{carb}}$ content at the Leibniz Laboratory for Radiometric Dating and Stable
196 Isotope Research (Kiel University, Germany) using a Kiel IV carbonate preparation
197 device connected to a ThermoScientific MAT 253 mass spectrometer. Precision of all
198 internal and external standards (NBS19 and IAEA-603) was better than $\pm 0.05\text{‰}$ for
199 $\delta^{13}\text{C}_{\text{carb}}$ and $\pm 0.09\text{‰}$ for $\delta^{18}\text{O}_{\text{carb}}$. All values are reported in the VPDB notation relative
200 to NBS19.

201 In addition, one sample from the central part of each bed ~~(19 samples)~~ was studied for
202 petrographic and scanning electron microscope (SEM) analysis, mineralogical content,
203 elemental composition and organic geochemistry. For the mineralogical and geochemical
204 analyses, the samples were ground in the laboratory. Whole-rock mineralogy was
205 obtained by analysing randomly oriented rock powder by X-ray diffraction (XRD), using
206 a Philips PW1710 diffractometer (Malvern Panalytical, Malvern, UK) at the University
207 of the Basque Country. The step size was 0.02° ~~2 θ~~ with a counting time of 0.5 s per step.
208 Major and trace element concentrations were determined at the University of the Basque
209 Country using a Perkin-Elmer Optima 8300 spectrometer (ICP-OES; PerkinElmer) and a
210 Thermo XSeries 2 quadrupole inductively coupled plasma mass spectrometer (ICP-MS;
211 Thermo Fisher Scientific) equipped with a collision cell, an interphase specific for
212 elevated total dissolved solids (Xt cones), a shielded torch, and a gas dilution system.
213 Analysis of the JG-2 granite standard and error estimates of each element showed that the
214 uncertainty of the results corresponds to the 95% confidence level. Finally, organic
215 carbon (C_{org}) and organic nitrogen (N_{org}) contents, as well as their isotopic $\delta^{13}\text{C}_{\text{org}}$ and
216 $\delta^{15}\text{N}_{\text{org}}$ values were obtained by combustion of powdered and decarbonated samples in
217 an elemental analyzer Flash EA 1112 (ThermoFinnigan) connected to a DeltaV
218 Advantage mass spectrometer (Thermo Scientific) at the University of A Coruña, Spain.
219 Calibration of $^{13}\text{C}_{\text{org}}$ and $^{15}\text{N}_{\text{org}}$ was done against certificated standards USGS 40,
220 USGS41a, NBS 22 and USGS24. Results are expressed in the VPDB notation, accuracy
221 (standard deviation) being $\pm 0.15\text{‰}$.

222 In order to explore compositional relationships and trends using comprehensive multi-
223 elemental datasets, Pearson correlation coefficients (r) and their significance (~~P~~ p -values)

224 were estimated for pairs of variables using the SPSS 28 statistical package (IBM
225 Corporation, SPSS statistics for Windows, version 28.0.1.1, 2022, Armonk, NY, USA).
226 In addition, a multivariate factor analysis was undertaken with the aim of identifying the
227 number of virtual variables (factors) that explains the highest percentage of the variability
228 in the analyzed dataset.

229 4. Results

230 4.1. General Santiurde section

231 4.1.1. Sedimentology and petrography

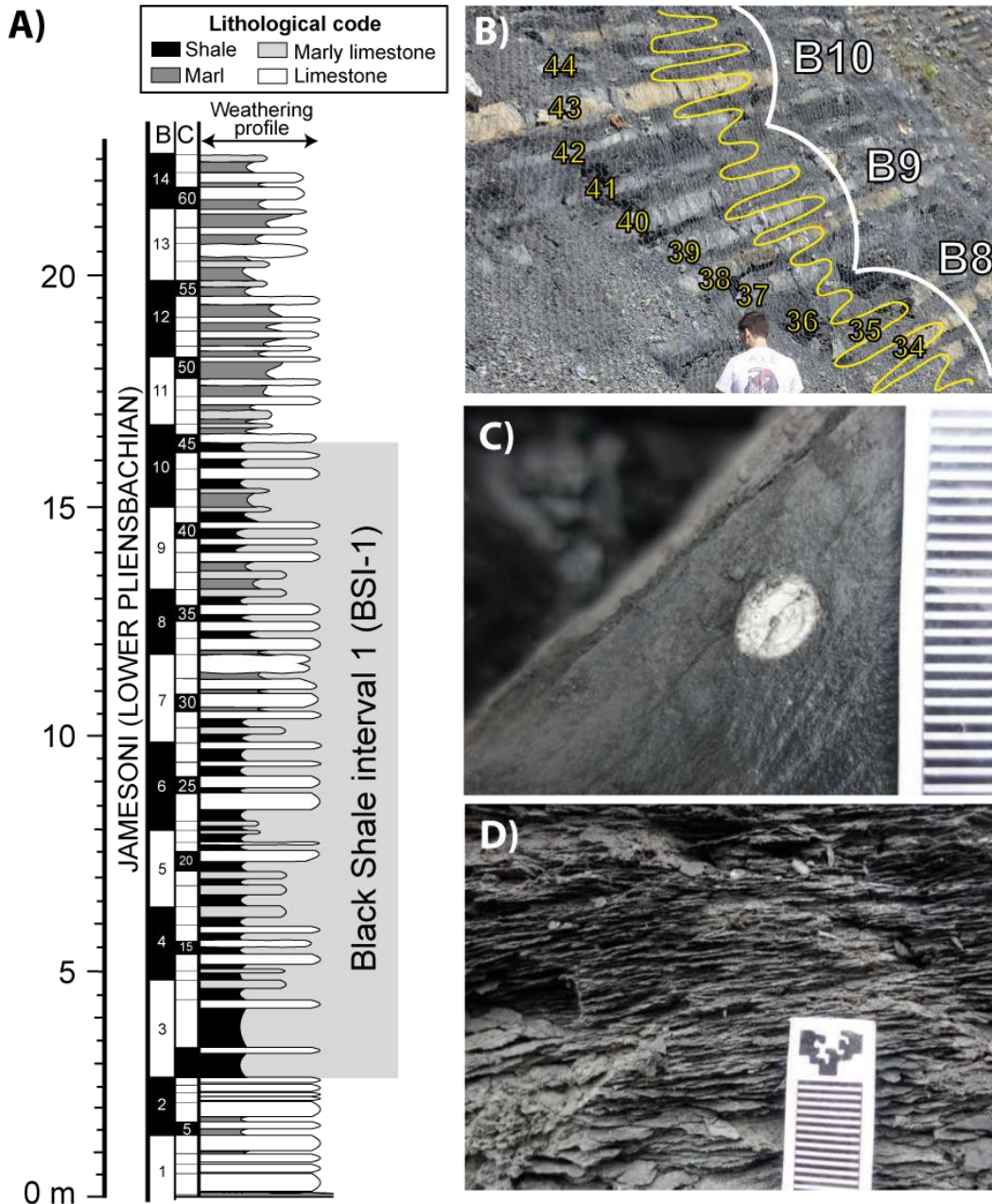
232 The ~~outcrop suecession~~ displays an ~~succession alternation~~ of ~~decimetre-scale plane-~~
233 ~~parallel beds, in which weather-resistant,~~ light coloured, bioturbated limestones or marly
234 limestone ~~beds resistant to weathering,~~ and ~~weather~~ alternate with ~~recessive,~~ dark
235 coloured, laminated marls or shales (Fig. 2). In the outcrop, ~~limestones and marly~~
236 ~~limestones were distinguished based on their hardness and colour, as prominent limestone~~
237 ~~beds are stiff and light grey, whereas marly limestones are less prominent, softer and~~
238 ~~show darker grey shades.~~ ~~the~~ The fossil record of ~~both~~ limestones and marly limestones
239 is dominated by isolated ammonites, belemnites and brachiopods (Fig. 2C), ~~and burrows~~
240 ~~attributable to *Chondrites* and *Planolites* have been observed.~~ Thin sections show
241 mudstones and wackestones with dispersed benthic foraminifera, fragmented
242 echinoderms, brachiopods and pyritized bivalve shells (mainly pectinids) in a microspar
243 matrix (Figs. 3A and C). Well-preserved placoliths of coccolithophorids ~~and calcispheres~~
244 were ~~also~~ identified by SEM (Figs. 3C and G). ~~Some signs of diagenetic overprinting~~
245 ~~were identified, such as the occurrence of secondary cements, calcite overgrowths, early~~
246 ~~framboidal pyrite and the growth of pyrite crystals in tests.~~

247 Both marls and shales constitute friable, ~~weather-recessive beds, more susceptible to~~
248 ~~weathering,~~ ~~the latter~~ Shales generally showing darker colour and more prominent
249 lamination (Fig. 2D), also observed in thin sections (Fig. 3B). ~~Furthermore,~~ ~~The~~ marls
250 contain nekto-planktonic fossils (ammonites, belemnite and calcareous unicellular algae)
251 and evidence of benthonic communities (pyritized shells of bivalves and rhynchonellid
252 brachiopods; trace fossils, such as *Chondrites* and *Planolites*), whereas the latter are
253 absent in shales. This is confirmed by SEM analysis, as marls contain isolated, broken
254 and randomly oriented clay minerals that wrap well-preserved coccoliths and calcispheres
255 with signs of bioturbation (Fig. 3C, 3D and 3G). Nektonic organisms and planktonic
256 unicellular algae also occur in shales, but benthonic fauna and bioturbation are virtually
257 absent. SEM observations also showed that the lamination in shales is caused by the
258 alternation of detrital components (mainly clays but also quartz) and organic components
259 (such as bitumen, polymeric extracellular substances linked to biofilms, filamentous
260 bacterial mats, or fungal hyphae; Fig. 3E and 3F). Pyrite fambroids are more common in
261 shales than in limy beds (Fig. 3H).

262 ~~The above mentioned lithologies were used to define characteristic intervals in the~~
263 ~~succession (Fig. 2A). Based on the occurrence of black shale layers, the BSI-1 spans from~~

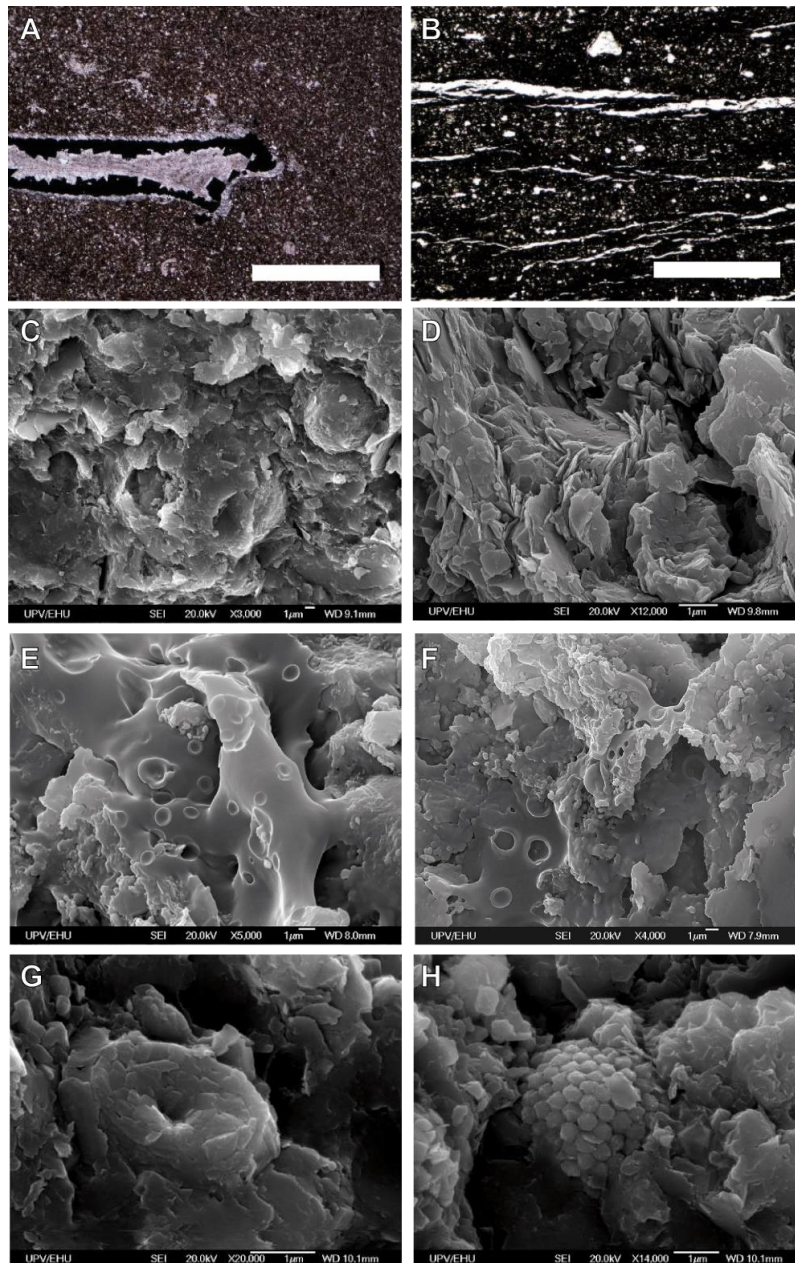
264
265
266

10.45 to 24.4 m (13.95 m thick). Black shales layers, with individual thicknesses of up to 79 cm, predominate in the lowermost part of the BSI, but intercalations of limestones, marly limestones and marls become progressively more abundant upsection.



267
268
269
270
271
272
273
274

Figure 2. A) Synthetic lithological log of the Santiurde section, including chronostratigraphy from Quesada et al. (2005) and Rosales et al. (2006). Columns B and C to the left of the lithological log correspond to bedding bundles and couplets, respectively, which were defined visually in the outcrop. B) Calcareous couplets (yellow numbers) of bundles 8 to 10 (white numbers) in the Santiurde outcrop. The white-yellow curve shows the relief of successive beds in the outcrop (left, weather-recessive; right, weather-resistant), which is mainly determined by their carbonate content. The white curve shows bedding bundles. C) Close up of a marly limestone with a partly pyritized belemnite. D) Close up of a laminated black shale. Scale bar in mm.



275
276
277
278
279

Figure 3. Petrographic views of limestone C41 (A) and shale C36 (B). The white bars represent 1 mm. C) General texture of a limestone bed (couplet C37), showing partly dissolved and broken coccoliths and calcispheres. D) General texture of a marly bed (couplet C37) with evidence of bioturbation. E) and F) probable biofilms. F) Well preserved coccolith. G) Pyrite fanbroid.

280

4.1.2. Bed arrangement

281

Cyclic bedding arrangements of different scales can be observed in the studied

282

lithological alternation. The term couplet refers to the lithological pair of a weathered

283

marl or shale bed and the overlying resistant limestone or marly limestone bed. A total of

284

62 calcareous bedding couplets (C1 to C62) were identified in the studied succession,

285

whose their individual thicknesses varying from 8 to 97 cm and averaging out at 36 cm

286

(Figs. 2A and 4). These couplets extend beyond the studied section, as shown by a bed-

287

by-bed correlation with the coeval railway section 1 km to the south-east (Fig. S1).

288 The lithological contrast between the marl/shale and the (marly) limestone of the couplets
289 is not constant throughout the succession, as some couplets are composed of shale and
290 limestone beds but others are constituted of marl and marly limestone beds. These
291 variations in the lithological contrast of couplets do not occur at random, but allow the
292 arrangement of the succession into bundles of five (four to six) couplets. These couplets
293 display a larger-scale arrangement in 12 complete bundles plus another two incomplete
294 bundles at the base and top of the section. These bundles range in thickness from 126 to
295 208 cm (average: 167.3 cm) and are composed of four to six couplets (generally five).
296 Bundles, as defined herein, typically contain a package of three prominent central
297 couplets (with significant-great lithological contrast between successive limestone and
298 marl/shale beds (e.g., couplets C34, C35, C38, C39, C40, C43 in Fig. 2B), which ~~is~~ are
299 underlain and overlain by less obvious couplets with (lower lithological contrast between
300 successive marl and marly limestone beds; (e.g., C36, C37, C41, C42 in Fig. 2B). In
301 Santiurde, 12 complete bundles plus another two incomplete bundles at the base and top
302 of the section were defined, which range in thickness from 126 to 208 cm (average: 167.3
303 cm).

304 Two successive bundles can be readily observed in some intervals of the studied
305 succession (e.g., B9 and B10 in Fig. 2B). However, the delimitation of bundles is not
306 straightforward in other equally thick intervals (Fig. S1). These intervals with well
307 defined and less obvious bundles alternate regularly throughout the Santiurde section,
308 which suggests the occurrence of a larger-scale (6.6 m thick) cyclic arrangement in the
309 lithological succession.

310 **4.1.2. 4.1.3. Colour, calcium carbonate and magnetic susceptibility**

311 Colour values (mean RGB) range from 69.87 to 158.99, averaging out at 102.73 (Fig. S1;
312 Table S1S2). The colour curve oscillates in line with the lithological alternation, colour
313 values generally being higher in limestones and marly limestones (average of 115.14)
314 than in intervening marls or shales (average of 90.71). The variations in colour values are
315 more-significant-greater in the central couplets of bundles than at bundle boundaries. This
316 suggests that, as shown in previous studies (Dinarès-Turell et al., 2018; Martínez-
317 Braceras et al., 2023), colour values are representative of the carbonate content of the
318 samples. This is confirmed by the carbonate content analysis carried out between couplets
319 C35 to C44 (see below), as both colour and carbonate content show the same arrangement
320 in couplets and bundles (r: 0.89, p<0.001; S1S2).

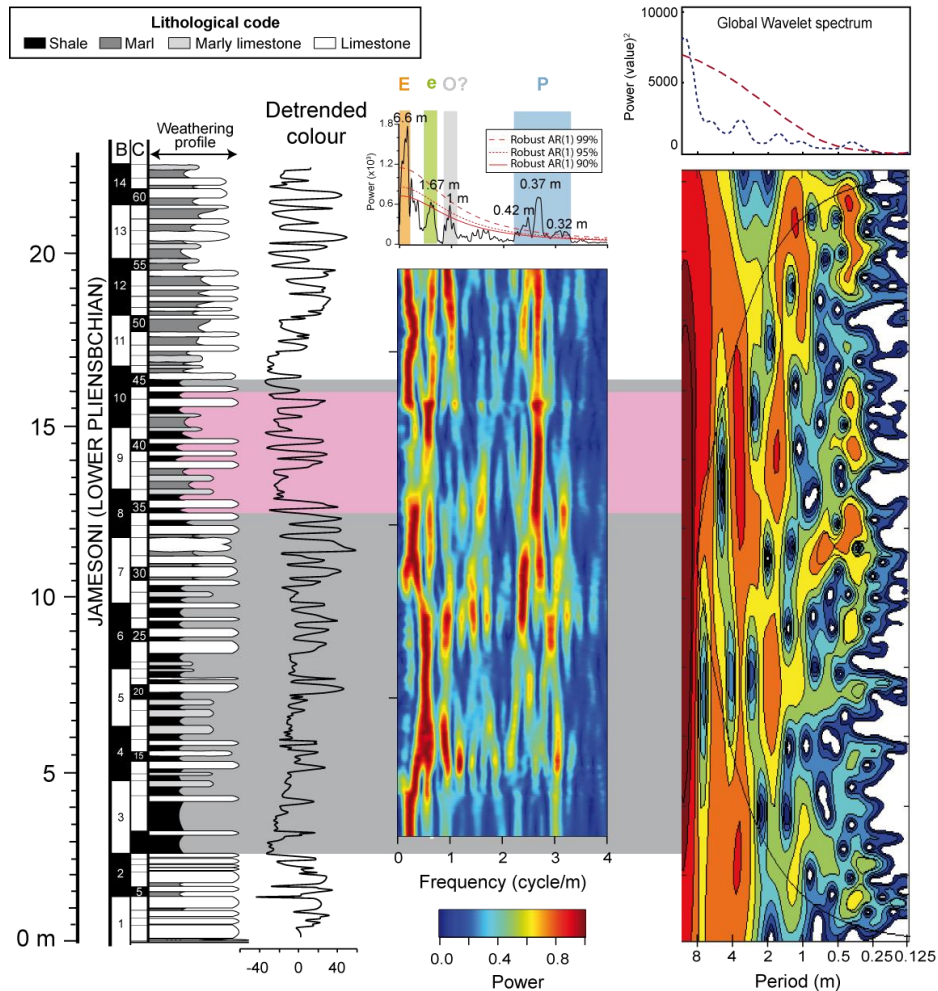
321 WeightMass-normalized magnetic susceptibility values range from 5.08×10^{-06} to
322 1.67×10^{-06} -05 m³/kg, averaging out at 9.9×10^{-06} m³/kg (Fig. S1S2, Table S1). In most
323 cases, limestones and marly limestones have higher susceptibility (average: 1.08×10^{-05}
324 m³/kg) than shales and marls (average: 8.99×10^{-06} m³/kg). The MS of hemipelagic
325 deposits is commonly determined by their paramagnetic components (mostly detrital
326 clays; Kodama and Hinnov, 2015). However, in Santiurde this parameter does not show
327 a great correlation with colour (r: 0.48, p<0.001, all section; Fig. S1S2) or calcium
328 carbonate (r: 0.36, p<0.001, between C35 and C44; Fig. S1S2). Therefore, the Santiurde

329 relationship suggests that the MS signal is more likely controlled by ferromagnetic
330 minerals, such as magnetite (Fig. [S2S3](#)).

331 **4.1.3.1. Time series analysis**

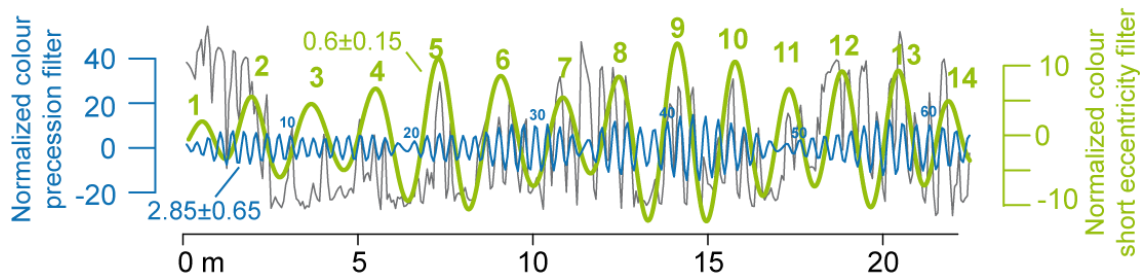
332 Prior to spectral analysis, the colour data series was regularly interpolated (spacing of
333 0.06 m) and the 3rd order polynomial trend was subtracted. The 2 π -MTM power spectrum
334 of the colour data series shows peaks at four period bands: 30-42 cm (peaking at 37 cm),
335 1 m, 1.67 m and 5-10 m (Fig. 4). The short period band shows significant peaks above
336 99% CL. In the intermediate period band, the 1 m peak exceeds 95% CL and the 1.67 m
337 peak reaches 90% CL. The long period band, with a main periodicity of which peaks at
338 6.6 m, is above 99% CL. The short period band matches the average thickness of couplets
339 and the longest intermediate band the average thickness of bundles. The EHA and wavelet
340 spectra also highlight the four main period bands, although the 1-m-periodicity is
341 relatively less relevant. The period bands are not continuous and there are several
342 intervals where the signal loses power, such as the 11-16 m and 24-36 m intervals of the
343 short period band. Spectral analysis carried out on MS data corroborate the prevalence of
344 the abovementioned four period bands, although the intermediate bands do not reach high
345 confidence levels (Fig. [S3S4](#)).

346 Using the average values of the period bands identified by spectral analysis, the The short
347 30-42 cm and long intermediate 1.6 m period components were separately extracted from
348 the colour data series through Gaussian bandpass filtering (Fig. 5), using the average
349 values of the period bands identified by spectral analysis (frequencies of 2.85 ± 0.65 and
350 0.6 ± 0.15 cycles/m, respectively). The number of oscillations in the shortest period filter
351 matches the number of couplets defined in the outcrop and in the colour curve. Similarly,
352 the oscillations in the intermediate period filter match the number and thickness of
353 bundles.



354
355
356
357
358
359
360
361
362

Figure 4. Stratigraphic log and chronostratigraphy (Quesada et al., 2005 and Rosales et al., 2006) of the studied section, showing the detrended colour curve. Bundles (B) and couplets (C) identified in the sedimentary alternation are numbered in ascending stratigraphic order. The grey background shows the extent of the Uptonia jamesoni ~~Block~~ ShaleBSI-1, and the pink interval in its upper part shows the interval studied herein in detail. The 2π-MTM, EHA and Wavelet spectra of the colour data series show the occurrence of four main period bands: 30–42 cm cycles (in blue in the 2π-MTM spectrum), interpreted as precession (P) couplets; 1 m cycles (grey), possibly related to obliquity (O?) cycles; 1.67 m cycles (green), representing short eccentricity (e) bundles; and 5–10 m cycles (peak at 6.76 m; orange), which corresponds to long eccentricity (E) bundles.



363
364
365

Figure 5. Colour filter outputs of short (in blue) and intermediate (green) period bands, which are related to precession couplets and short eccentricity bundles respectively.

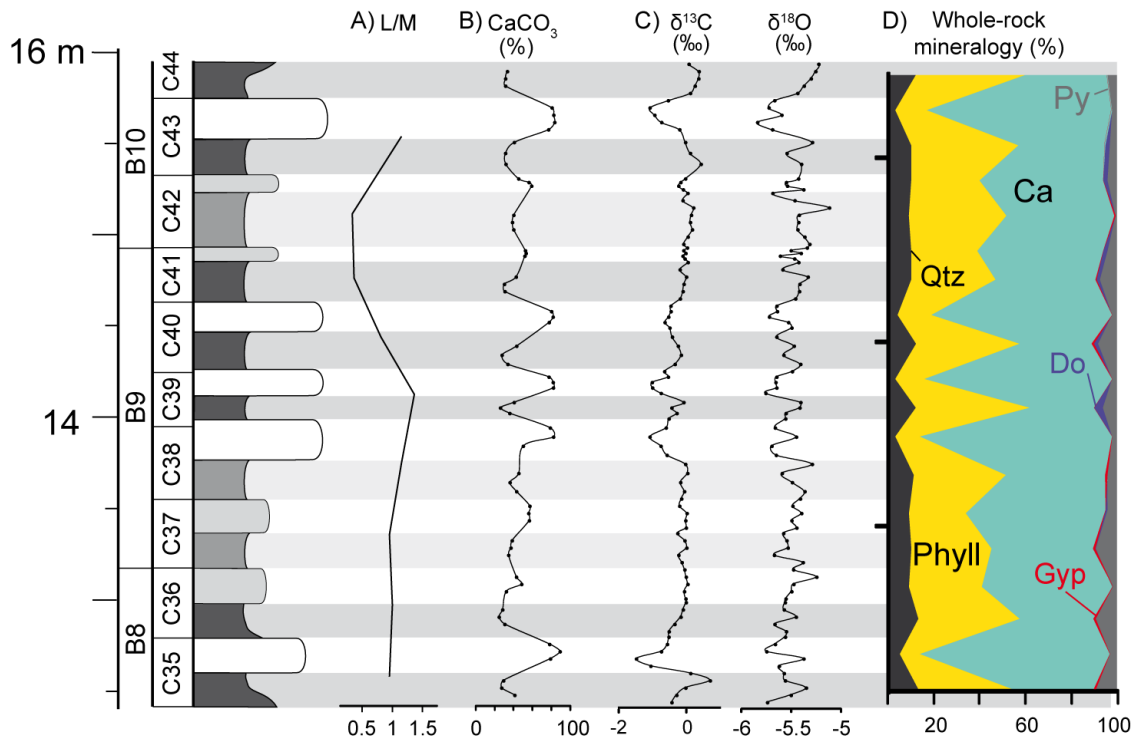
366 4.2. Detailed analysis of Bundle 9 (C35–C44 interval)

367 4.2.1. L/M ratio and calcium carbonate content

368 The limestone/marlstone (L/M) thickness ratio of couplets varies between 0.33 (C42) and
369 1.36 (C39), with an average value of 0.90 (Fig. 6A, Table S2). The highest L/M values

370 are found in the couplets at the central part of bundle B9, while the lowest values
 371 correspond to couplets C41 and C42, at the boundary between bundles B9 and B10.

372 The CaCO_3 content ranges from 24.63 to 88.97%, averaging out at 49.78% (Fig. 6B;
 373 Table S3). **In general, % CaCO_3 fluctuates in line with the visually defined lithology,**
 374 **limestones and marly limestone beds (average: 66.36%) being richer in % CaCO_3**
 375 **(average: 66.36%)** than marls and shales (average: 34.86%). Marls and shales differ by
 376 10-15% in their CaCO_3 content, whereas limestone beds at the central part of bundle B9
 377 show 20-40% more CaCO_3 than **counterpart** marly limestones at bundle boundaries.



378 Figure 6. Lithological log of the Santiurde interval studied in detail (dark grey: shale; ~~pale-intermediate~~ grey: marl;
 379 ~~light grey: marly limestone; white: limestone and marly limestone~~), showing (A) the limestone–marl (L/M) thickness
 380 ratio of couplets, (B) % CaCO_3 content, (C) $\delta^{13}\text{C}_{\text{carb}}$ and $\delta^{18}\text{O}_{\text{carb}}$ curves and (D) whole-rock mineralogy. Numbered
 381 couplets and bundles are labelled C and B, respectively. ~~The 0 m level corresponds to 20.34 m of the general section.~~
 382

383 4.2.2. Carbon and oxygen isotopes

384 $\delta^{13}\text{C}_{\text{carb}}$ values range from -1.5 (C35L) to 0.70‰ (C35M) and average out at -0.25‰ (Fig.
 385 6C). The $\delta^{13}\text{C}_{\text{carb}}$ curve shows lower values in limy beds and higher values in shales and
 386 marls. The amplitude of the fluctuations is significantly greater in the central couplets of
 387 bundle B9. $\delta^{18}\text{O}$ values range from -5.84 (C43L) to -5.25‰ (C36L) and average out at -
 388 5.52‰, the $\delta^{18}\text{O}$ curve being rather spiky. $\delta^{13}\text{C}_{\text{carb}}$ and $\delta^{18}\text{O}_{\text{carb}}$ data show intermediate
 389 positive correlation ($r: 0.53; p < 0.005$; Fig. ~~S4AS5A~~; Table S3).

390 4.2.3. General mineralogy

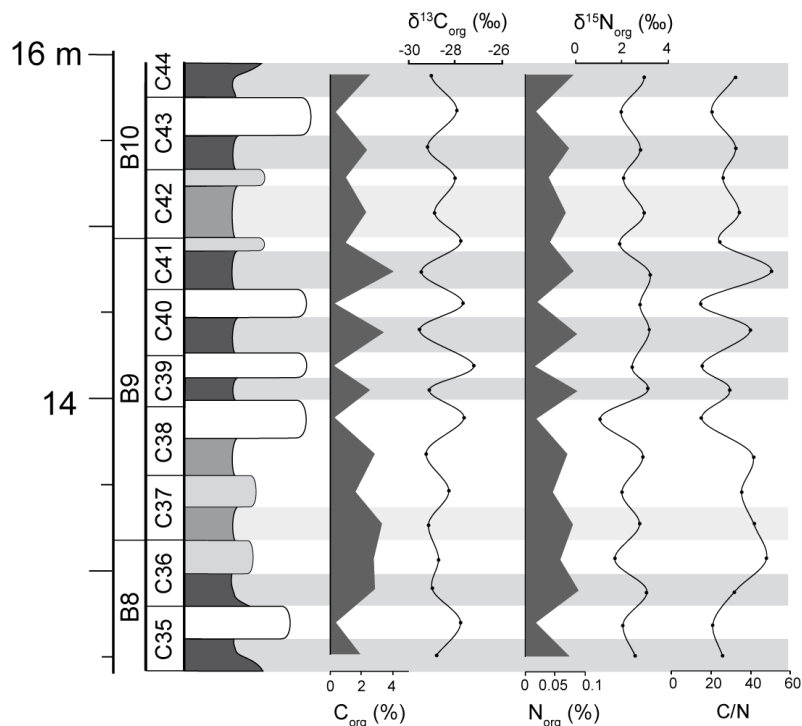
391 XRD results (Fig. 6D; Table S2) show that calcite is the most abundant mineral in limy
 392 beds and in some of the marl/shales (28 to 84%, average: 54%). Clay minerals constitute
 393 the second most abundant phase (9 to 50%, average: 32%), followed by quartz (3 to 13%,
 394 average: 9%) and other minor components (pyrite, gypsum, and dolomite).

395 The mineralogical content fluctuates in line with lithology, as it shows maximum values
 396 of clays and quartz, and minima of calcite, in marls/shales. Moreover, the amplitude of
 397 the detrital/carbonate mineralogical oscillations increases in the central couplets of bundle
 398 B9. Pyrite, despite being a minor component (0.5 to 9%, average: 4%), also oscillates
 399 with lithology, presenting maximum values in marls/shales, but does not match the
 400 amplitude variation associated with the bundle arrangement.

401 4.2.4. Organic matter geochemistry

402 The content in organic carbon varies between 0.26 (C39L) and 4.03% (C41M) (average
 403 of 1.91%), **with** maximum values being found at black shales. Organic nitrogen also
 404 covaries with lithology, with values ranging from 0.02 (C39L) to 0.09 % (C36M)
 405 (average of 0.06%). Both elements show high amplitude oscillations at the central part of
 406 bundle B9 and subdued oscillations at bundle boundaries. The relationship between both
 407 organic components was calculated by the C/N ratio (Fig. 7; Table S2)

408 $\delta^{13}\text{C}_{\text{org}}$ values vary between -29.6 (C40M) and -27.2‰ (C40L), and average out at -
 409 28.6‰. $\delta^{15}\text{N}_{\text{org}}$ ranges from 1.1 (C38L) to 3.2‰ (C40M), with an average value of 2.5‰
 410 (Fig. 7). Both data series alternate in line with lithology, but with opposite trends. The
 411 $\delta^{13}\text{C}_{\text{org}}$ fluctuations at the central couplets of bundle B9 show the greatest amplitude.

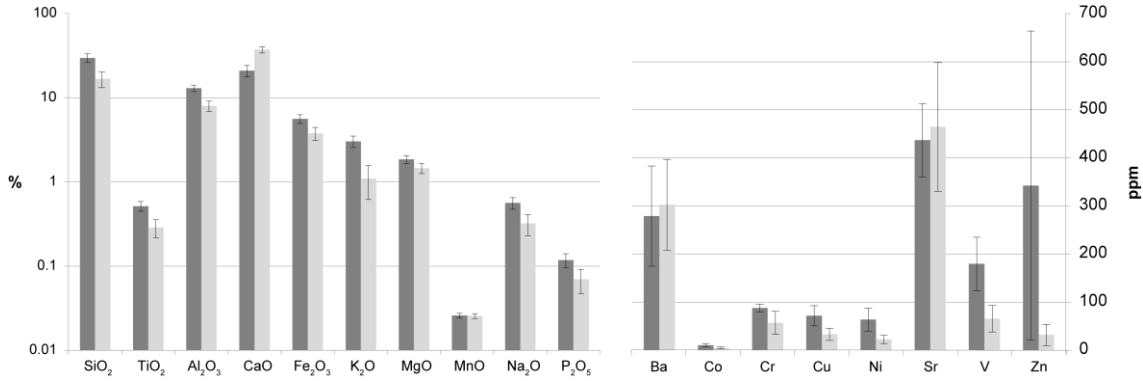


412
 413 Figure 7. Lithological log of the Santiurde interval studied in detail, showing fluctuations in the percentage of organic
 414 C and N, C/N ratio, $\delta^{13}\text{C}_{\text{org}}$ and $\delta^{15}\text{N}_{\text{org}}$.

415 4.2.5. Elemental geochemistry

416 The average abundance of major and trace elements is shown in Fig 8 (Table S4). SiO_2 ,
 417 Al_2O_3 and CaO constitute 48% of limestones and 63% of marls/shales. Average values
 418 of most major and trace elements are higher in marls and shales than in limy beds, the
 419 exceptions being CaO , MnO , Ba and Sr . The correlation matrix shows that the abundance

420 of MnO does not correlate with any major and trace elements, but all the other major
 421 elements present strong negative correlation (>-0.88) with CaO (Table 1) and high
 422 positive correlation with most redox sensitive trace elements (Co, Cu, Ni, V and Zn), the
 423 only exception being Zn, which shows intermediate positive correlations. Sr and Ba
 424 display intermediate positive correlation with each other.



425
 426 Figure 8. The average abundance of major and trace elements of limestones (pale grey) and marl/shales (dark grey).

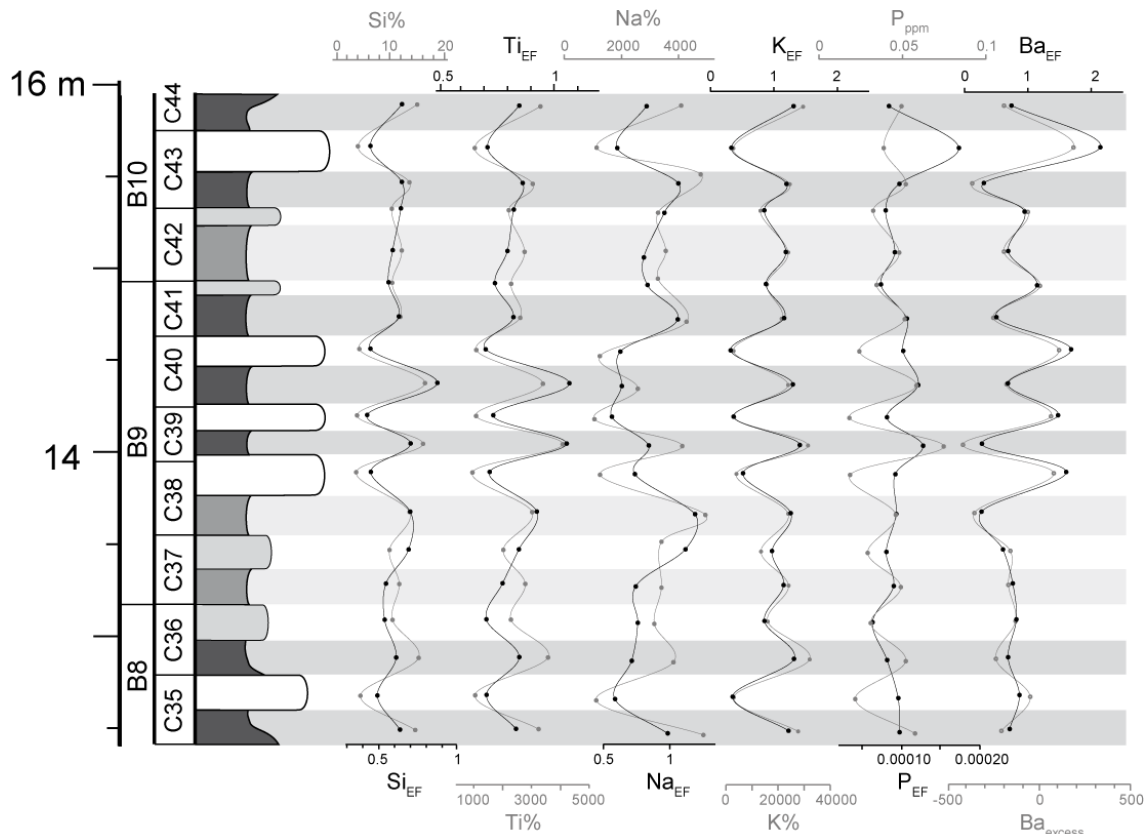
	SiO ₂	TiO ₂	Al ₂ O ₃	CaO	Fe ₂ O ₃	K ₂ O	MgO	MnO	Na ₂ O	P ₂ O ₅	Ba	Co	Cr	Cu	Ni	Sr	V	Zn
SiO ₂		9.9E-15	1.2E-09	9.2E-16	5.8E-07	1.3E-11	2.9E-07	0.97	2.3E-06	1.1E-06	6.1E-01	2.6E-07	2.0E-10	2.1E-06	4.3E-05	5.8E-01	2.8E-03	2.3E-02
TiO ₂	0.99		4.0E-10	4.2E-15	4.3E-08	9.4E-14	7.1E-08	0.80	4.8E-06	7.0E-08	5.6E-01	7.5E-07	2.2E-09	8.4E-06	7.9E-05	6.5E-01	8.9E-04	2.0E-02
Al ₂ O ₃	0.94	0.95		1.4E-12	6.2E-09	1.3E-12	2.8E-06	1.00	5.4E-07	1.7E-05	9.1E-01	3.2E-04	4.7E-09	5.1E-04	1.1E-03	3.5E-01	1.9E-04	1.4E-02
CaO	-0.99	-0.99	-0.98		1.4E-08	5.3E-15	1.8E-07	0.96	5.7E-07	9.5E-07	6.6E-01	4.7E-06	2.4E-11	9.4E-06	6.2E-05	5.5E-01	4.4E-04	1.7E-02
Fe ₂ O ₃	0.88	0.91	0.93	-0.93		6.2E-09	1.8E-06	0.57	7.4E-07	8.1E-06	6.9E-01	1.1E-03	1.1E-06	3.3E-04	6.2E-04	8.2E-01	4.5E-06	1.0E-02
K ₂ O	0.97	0.98	0.98	-0.99	0.93		1.8E-06	0.97	1.1E-06	6.1E-07	7.1E-01	1.7E-05	4.5E-09	3.6E-05	1.3E-04	6.9E-01	1.3E-04	1.2E-02
MgO	0.89	0.91	0.86	-0.90	0.86	0.86		0.10	0.00	0.00	0.52	0.00	0.00	0.00	0.00	0.67	0.00	0.14
MnO	-0.01	0.06	0.00	-0.01	0.14	0.01	0.39		0.85	0.62	0.68	0.77	0.75	0.60	0.75	0.82	0.46	0.22
Na ₂ O	0.86	0.85	0.88	-0.88	0.88	0.87	0.79	0.05		0.00	0.34	0.01	0.00	0.00	0.00	0.90	0.00	0.02
P ₂ O ₅	0.87	0.91	0.82	-0.87	0.84	0.88	0.80	0.12	0.72		0.53	0.00	0.00	0.00	0.00	0.58	0.00	0.01
Ba	-0.13	-0.14	0.03	0.11	-0.10	-0.09	-0.16	-0.10	-0.23	-0.16		0.43	0.55	0.24	0.26	0.00	0.29	0.91
Co	0.89	0.88	0.74	-0.85	0.69	0.82	0.75	-0.07	0.61	0.85	-0.19		7E-05	1E-09	5E-07	7E-01	8E-02	2E-02
Cr	0.96	0.94	0.93	-0.97	0.87	0.93	0.91	0.08	0.88	0.80	-0.15	0.79		0.00	0.00	0.66	0.00	0.10
Cu	0.86	0.84	0.72	-0.83	0.74	0.80	0.71	-0.13	0.69	0.84	-0.28	0.94	0.77		1E-09	1E+00	2E-02	4E-03
Ni	0.80	0.78	0.69	-0.79	0.71	0.77	0.67	-0.08	0.65	0.78	-0.27	0.88	0.75	0.95		0.9	0.0	0.0
Sr	0.14	0.11	0.23	-0.15	0.06	0.10	0.11	0.05	-0.03	0.14	0.65	0.08	0.11	-0.01	-0.04		0.49	0.98
V	0.65	0.70	0.76	-0.73	0.85	0.77	0.65	0.18	0.82	0.65	-0.26	0.42	0.71	0.52	0.62	-0.17		0.02
Zn	0.52	0.53	0.55	-0.54	0.57	0.56	0.35	-0.29	0.52	0.59	-0.03	0.53	0.39	0.62	0.65	0.01	0.52	

427
 428 Table 1. Pearson correlation coefficient (r) of major and trace element concentrations in the lower left part of the matrix.
 429 The p-value for each coefficient is located in the upper right part of the matrix. Highest ($r > \pm 0.65$) correlations are
 430 marked in bold and intermediate correlations ($r \geq \pm 0.50-0.64$) in bold and italics.

431 In order to compare the abundance of some elements with the reference average shale
 432 composition (Li and Schoonmaker, 2003), enrichment factors (X_{EF} ; Tribovillard et al.,
 433 2006) were calculated as follows: $X_{EF} = (X/Al)_{\text{sample}} / (X/Al)_{\text{average shale}}$. Al and K are
 434 commonly thought to be related to the clay fraction, whereas Si and Ti are often
 435 associated with the coarser fraction of quartz and heavy minerals (Calvert and Pedersen,
 436 2007). Enrichment in Ti has also been related to stronger aeolian input (Rachold and
 437 Brumsack, 2001). In Santiurde K_{EF} , Ti_{EF} and Si_{EF} covary with lithology, showing
 438 maximum values in marls/shales and increasing **amplitude of variability the amplitude of**
 439 **the oscillations** in the middle part of bundle B9 (Fig. 9).

440 Marine palaeoproductivity is commonly associated with algal growth, which varies with
 441 the availability of macro-nutrients, such as P and N (Calvert and Pedersen, 2007). P_{EF}
 442 values from Santiurde show that these deposits are depleted in P (Li and Schoonmaker,
 443 2003). However, P_{EF} shows higher values in marls/shales than in limy beds in almost all

444 couplets (except in C35L and C43L; Fig. 9). Authigenic Ba in marine sediments is
 445 commonly associated to barite and its abundance is generally determined by organic C
 446 export from surface **waterswater** into deep marine environments (Tribovillard et al.,
 447 2006). In order to minimize the influence of detrital barium in palaeoenvironmental
 448 analyses, Ba_{EF} and the Ba_{excess} index are widely used (Dymond et al., 1992). Ba_{EF} shows
 449 that the studied succession is significantly depleted in Ba in comparison with average
 450 shales (Fig. 9, Li and Schoonmaker, 2003). Both Ba_{EF} and Ba_{excess} reveal increased
 451 accumulation of Ba when OM-poor limestones were deposited, just the opposite of P_{EF} .

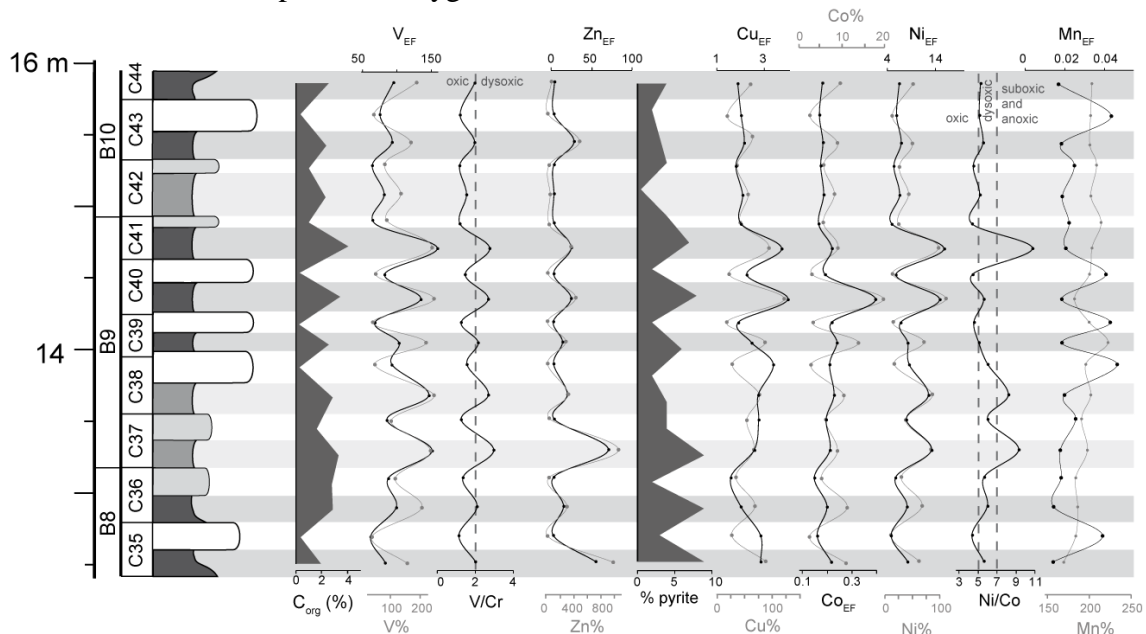


452
 453 Figure 9. Lithological log of the Santiurde interval studied in detail, showing fluctuations in the percentage of elements
 454 related to detrital input (Si, Ti, Na and K), palaeoproductivity (P and Ba) and their enrichment factors (EF). The Ba_{excess}
 455 ratio is also presented.

456 Mn_{EF} is commonly linked to authigenic Mn phases, such as authigenic oxi-hydroxides.
 457 In Santiurde Mn_{EF} shows an oscillatory pattern in line with lithology, with maximum
 458 values at limestones (Fig. 10). As no evidence of Pliensbachian hydrothermal or volcanic
 459 activity has been reported to date in the area, the higher Mn_{EF} in limestones could suggest
 460 increased terrestrial input, more oxygenated deep **waterswater** or increased
 461 remineralization of organic matter (Bayon et al., 2004; Tribovillard et al., 2006; Calvert
 462 and Pedersen, 2007). Both V and Zn commonly show a strong association with OM
 463 content (Calvert and Pedersen, 2007; Algeo and Liu, 2020). The type of organic matter
 464 affects the distribution of both elements, as V is taken up by tetrapyrrole complexes
 465 derived from chlorophyll decay, whereas Zn is known to be incorporated into humic and
 466 fulvic acids (Lewan, 1984, Aristilde et al., 2012). Enrichment factors of both elements
 467 show oscillatory patterns in line with lithology, with maximum values at shales/marls and
 468 a significant enrichment in V (Fig. 10). On the other hand, Co, Cu and Ni are known to

469 be related with sulphide fractions (Tribovillard et al., 2006; Algeo and Liu, 2020), as these
 470 elements are usually incorporated as minor constituents in diagenetic pyrite (Berner et al.,
 471 2013). With the exception of Cu_{EF} , the enrichment factors of these elements also fluctuate
 472 with the lithological alternation, showing maximum values in shales/marls (Fig. 10).

473 Several bioelemental ratios associated with redox conditions during sedimentation were
 474 also calculated. According to absolute values of the V/Cr bioelemental ratio, most marls
 475 and shales were deposited under dysoxic conditions, whereas limestones and marly
 476 limestones were accumulated in oxic conditions (Fig. 10; Jones and Manning, 1994).
 477 Ni/Co values from marls and shales support dysoxic or even suboxic/anoxic conditions
 478 (Fig. 9, Jones and Manning, 1994), but suggest that limestones and marly limestones also
 479 accumulated in nearly dysoxic conditions. The discrepancy between V/Cr and Ni/Co
 480 results confirms the limitation of absolute-these bioelemental ratios to discriminate
 481 absolute redox conditions (Algeo and Liu, 2020). In Santiurde all lithologies are enriched
 482 in V, Zn, Ni and Cu when compared with average shales (Li and Schoonmaker, 2003).
 483 The concentration of these redox-sensitive trace elements is generally higher than in
 484 crustal rocks when sediments accumulate under oxygen depleted conditions (Brumsack,
 485 1986; Arthur et al., 1990). Consequently, it is assumed that deep seawater oxygen
 486 concentrations was-were fluctuating, but the general background conditions of the
 487 environment were depleted in oxygen.

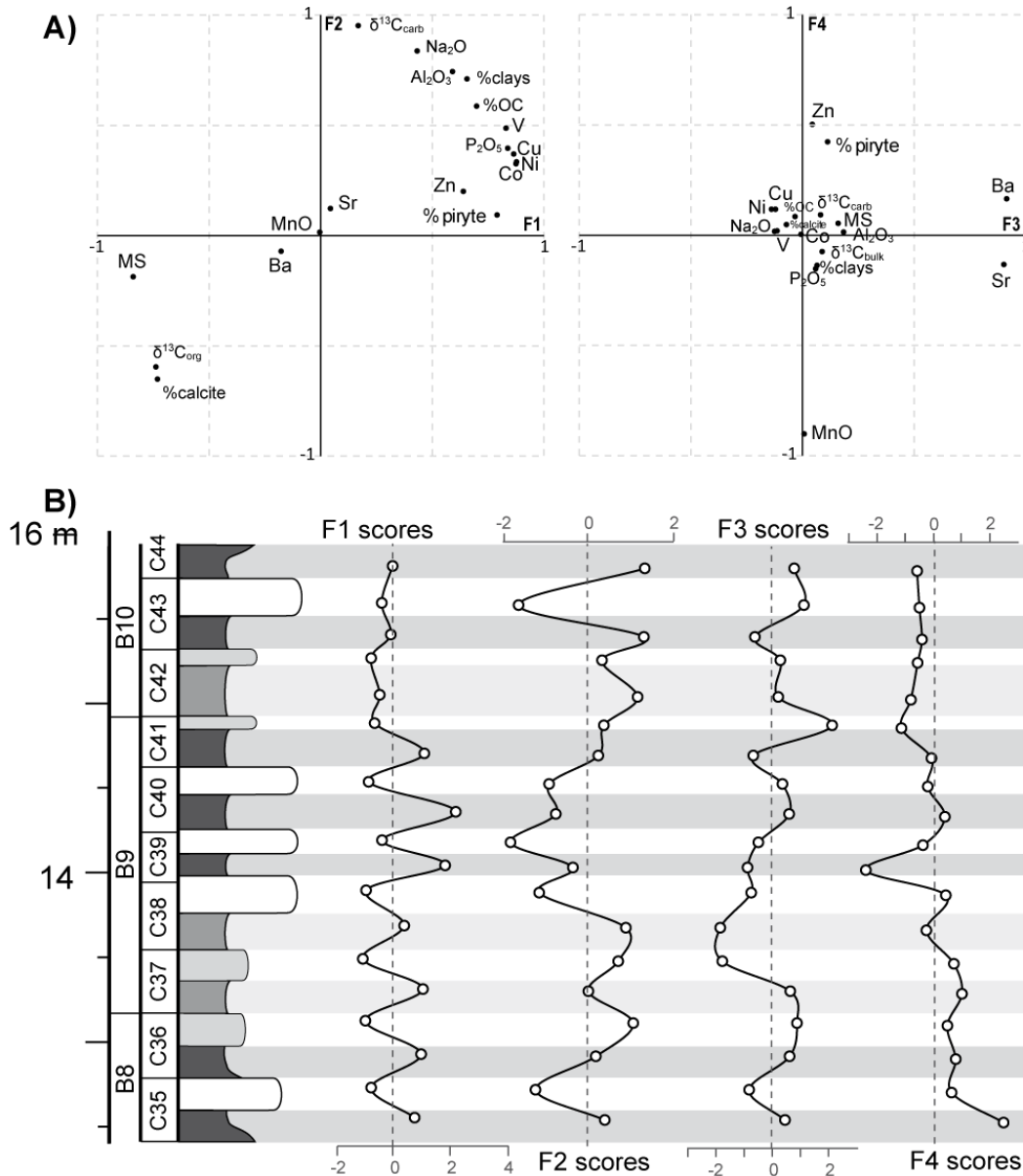


488
 489 Figure 10. Lithological log of the Santiurde interval studied in detail, showing fluctuations in the percentage of redox
 490 sensitive elements, their EFs and several bioelemental ratios, along with the organic carbon and pyrite content.

491 4.2.6. Factor analysis

492 A statistical factor analysis was conducted in order to identify key groups of variables
 493 with similar trends in the mineralogical and geochemical databases. As the number of
 494 variables introduced in the analysis has to be lower than the number of cases (19 samples),
 495 a total of 18 variables of the total dataset were selected had to be reduced to 18 variables.
 496 To this end, vVariables with no quantifiable concentrations throughout the studied section
 497 (e.g., gypsum and dolomite content) were also excluded. eElements with very strong

498 mutual correlation coefficients (for example, Mg and Fe with Al) were also ignored,
 499 because they would yield redundant data and increase the size of the dataset. Main redox
 500 sensitive elements, in whose-which Santurde is enriched, have been included because of
 501 their palaeoenvironmental significance. ~~Variables with no quantifiable concentrations~~
 502 ~~throughout the studied section (e.g., gypsum and dolomite content) were also excluded.~~
 503 Thus, the analysed dataset consists of 18 variables (see Table S5 and Fig. 11) from 19
 504 cases (beds).



505
 506 Figure 11. A) Projection of different elements in the Factor 1 versus Factor 2 cross-plot (ca. 70% of the total variance)
 507 and in the Factor 3 versus Factor 4 cross-plot (ca. 18% of the total variance). B) Stratigraphic distribution of factorial
 508 scores of the four extracted factors (virtual variables).

509 The optimal factor analysis (varimax rotation) extracted four factors (F1 to F4) or virtual
 510 variables that have eigenvalues greater than one. These factors explain 87.97% of the
 511 cumulative variance of the analyzed data matrix (Fig. 11 and Table S5). Factors 1 and 2
 512 explain the highest percentage of the dataset, 44.54% and 25.78% respectively. Both
 513 factors explain the variance of variables linked to the lithological alternation and the

514 arrangement of couplets in bundles (Fig. 11). F1 shows higher loadings for variables
515 linked to oxygenation state (trace elements, pyrite, C_{org} vs $\delta^{13}C_{org}$, MS) and
516 palaeoproductivity (P_2O_3). Conversely, F2 has higher loadings in variables (Na_2O , Al_2O_3 ,
517 clay% vs calcite) linked to the dilution of calcite with terrigenous material; $\delta^{13}C_{carb}$ also
518 shows a very high positive loading with F2. Factors 3 and 4 explain a significantly lower
519 variance of the total dataset, 9.92 and 7.73% respectively. F3 shows very high positive
520 loadings for Ba and Sr, whereas F4 shows very high negative loadings for MnO and
521 intermediate positive loading for Zn and pyrite. The scores of factors 3 and 4 do not align
522 with the lithological arrangement in couplets and bundles, which suggests that they were
523 not controlled ~~by the same mechanisms that produced the calcareous rhythmites orbitally~~
524 ~~influenced environmental conditions that produced the calcareous rhythmites.~~

525 5. Discussion

526 5.1. Origin of ~~the inorganic~~ sedimentary fluctuations

527 5.1.1. Santiurde ~~rhythmites~~: primary or diagenetic?

528 Previous studies have shown that the formation of calcareous ~~rhythmites~~ can be
529 caused by both primary and diagenetic processes. In some cases, ~~rhythmites~~ have
530 been considered to be primary, being related to secular variations in the environmental
531 conditions that controlled sedimentation (e.g., Arthur and Dean, 1991; Hinnov and Park,
532 1999; Dinarés-Turell et al., 2018; Martínez-Braceras et al., 2023). In other cases,
533 postdepositional dissolution/cementation processes have been considered the most
534 important (e.g., Hallam, 1986; Reuning et al., 2002; Westphal, 2006; Nohl et al. 2021).
535 When differential diagenesis affects the primary composition of sediments, part of the
536 carbonate dissolves from marly beds and migrates to limy beds, precipitating as cements
537 (Westphal, 2006).

538 ~~The Santiurde deposits show some signs of diagenetic overprinting, such as the~~
539 ~~occurrence of some secondary cements, calcite overgrowths, early framboidal pyrite and~~
540 ~~the growth of pyrite in tests (Fig. 3). In fact, ~~t~~he aragonitic and high-Mg calcite~~
541 components of limestones, including their micritic matrix, suffered significant re-
542 crystallization. However, none of the limestone beds displays a nodular geometry, which
543 is common in successions affected by intense postdepositional dissolution/cementation
544 processes (Hallam, 1986; Einsele and Ricken, 1991). Quite the opposite, the
545 characteristics of the beds are continuous for more than 1 km ~~as shown by bed-by-bed~~
546 ~~correlation between the Santiurde section studied herein motorway and the railway~~
547 ~~sections studied by others (Rosales et al., 2001, 2004, 2006; Quesada et al., 2005; Fig.~~
548 ~~S1).~~ Furthermore, petrographic and SEM observations suggest that fluid migration from
549 marly to limy beds was overall limited. Thus, skeletal components of marls/shales (Fig.
550 2 and 3) do not present features of increased compaction (Munnecke et al., 2001;
551 Westphal, 2006). This was probably related to an original higher clay content in
552 marls/shales, which hampered fluid migration between beds and ~~avoided-prevented~~
553 intense dissolution and recrystallization. In addition, clay minerals show primary textures
554 (such as deformed, broken plates or isolated flakes wrapping other detrital grains), but do

555 not show any evidence of intense diagenetic recrystallization. ~~In general, the diagenetic~~
556 ~~characteristics observed in the Santiurde rhythmites are typical of processes related to~~
557 ~~organic matter decay during burial (Rosales et al., 2001).~~

558 Interestingly, the lithological arrangement in couplets and bundles observed in the
559 outcrop, combined with the spectral analysis of colour and MS data series, highlight the
560 presence of sedimentary cycles with three main periodicities in the succession
561 (6.6:1.67:0.36). This ratio is comparable to the 405:100:20 ratio produced by the
562 superposition of long eccentricity, short eccentricity and precession cycles (Berger and
563 Loutre, 1994). ~~Unfortunately, the available chronostratigraphic framework (Braga et al.,~~
564 ~~1988; Fraguas et al., 2015) does not provide the resolution required to confirm the~~
565 ~~duration of the sedimentary cycles.~~

566 The abovementioned characteristics strongly suggest that the formation of the Santiurde
567 rhythmites was primary and responded to orbitally driven climate change episodes. An
568 orbital control on sedimentation had previously been deduced in other Pliensbachian
569 successions from nearby areas, such as the Asturian and Iberian basins (Bádenas et al.,
570 2012; Val et al., 2017; Sequero et al., 2017).

571 **5.1.21. Preservation of the geochemical signal**

572 Although the formation of the Santiurde ~~rhythmites~~ ~~rhythmites~~ was a result of orbitally
573 paced environmental variations, some primary sedimentary characteristics (such as
574 chemical and mineralogical composition, fossil assemblage, or porosity) could have
575 responded in different ways to diagenesis. Consequently, the geochemical data of the
576 seven limestone-marl couplets (C35-C44) studied in detail must be analyzed carefully in
577 order to interpret which environmental variations controlled sedimentation.

578 Whole-rock inorganic isotopic analyses from diagenetically “closed” systems, such as
579 hemipelagic carbonates, have been used successfully for the climatic reconstruction of
580 ancient sedimentary environments (e.g., Jenkyns and Clayton, 1986; Marshall, 1992;
581 Silva et al., 2011; Martínez-Braceras et al., 2017; Deconinck et al., 2020). However,
582 $\delta^{13}\text{C}_{\text{carb}}$ and $\delta^{18}\text{O}_{\text{carb}}$ values tend to get depleted during burial, causing a significant
583 positive correlation between each other when strong deep burial ~~or meteoric~~ diagenesis
584 affects the succession (Banner and Hanson, 1990; Marshall, 1992; Swart, 2015). In
585 Santiurde both isotopic records show depleted values in comparison to Early Jurassic
586 marine isotopic standard curves (Grossman and Joachimski, 2020; Cramer and Jarvis,
587 2020). Both $\delta^{18}\text{O}_{\text{carb}}$ and $\delta^{13}\text{C}_{\text{carb}}$ records show a positive but not very high correlation
588 (Fig. [S4A5A](#); $r: 0.53, p < 0.005$), following a common burial trend (Banner and Hanson,
589 1990). This suggests that, although primary isotopic trends may have been preserved,
590 absolute values are probably distorted. Accordingly, $\delta^{18}\text{O}_{\text{carb}}$ values from Santiurde are
591 significantly depleted (Grossman and Joachimski, 2020) and display a spiky curve (Fig.
592 6). This may reflect the impact of the percolation of diagenetic fluids in post-depositional
593 processes at low fluid/rock ratios (Banner and Hanson, 1990). Consequently, $\delta^{18}\text{O}_{\text{carb}}$
594 values were only used to assess the degree of diagenetic ~~overprinting of other~~
595 ~~geochemical proxies.~~

596 Rosales et al. (2001) analyzed the utility of stable isotopes from Lower-Middle Jurassic
597 bulk hemipelagic carbonates and fossils (belemnites and brachiopods) from the BCB as
598 palaeoceanographic proxies. They concluded that whole rock stable isotope records from
599 Lower-Middle Jurassic hemipelagic carbonates from the BCB are not suitable for
600 accurate palaeoceanographic reconstructions because their high OM content contributed
601 to the alteration of their primary signal. In fact, organic matter degradation and sulphate
602 reduction in deep sea sediments is known to produce CO₂ enriched in ¹²C and generate
603 early cements with low δ¹³C_{carb} (Dickson et al., 2008; Swart, 2015). Accordingly, the
604 generally depleted δ¹³C_{carb} values in Santiurde could be a consequence of the addition of
605 early cements precipitated in equilibrium with isotopically light pore waters affected
606 by OM decay. This process, however, cannot explain the δ¹³C_{carb} fluctuations observed
607 along the lithological alternation, because the influence of δ¹³C-depleted fluids is
608 generally thought to be more pronounced when carbonate content in the sediment is low
609 and the total organic carbon is comparatively high (Ullman et al., 2022). Contrarily, in
610 Santiurde maximum δ¹³C_{carb} values are recorded in marls/shales and the crossplot of
611 δ¹³C_{carb} versus CaCO₃ values shows a high negative correlation (r: -0.75, p<0.005; Fig.
612 S4B5B). It can therefore be assumed that the high clay content and low porosity in
613 marls/shales probably hampered a more intense cementation during early diagenesis
614 (Arthur and Dean, 1991).

615 In line with the above argumentation, δ¹³C_{carb} records of hemipelagic carbonates are
616 commonly used in palaeoclimatic studies because they are not strongly affected by the
617 bicarbonate composition and temperature of interstitial waters (Marshall, 1992;
618 Mackensen and Schmiedl, 2019). However, Additionally, dissolution of aragonite and
619 high-Mg calcite components, which are generally more abundant in shallow marine areas,
620 and precipitation of more stable low-Mg calcite phases are important post-depositional
621 process causing carbon isotope fractionation (Reuning et al., 2002). Aragonite is
622 generally characterized by more positive δ¹³C values than high- or low-Mg carbonates
623 (Swart, 2015). Therefore, a fluctuating rate of aragonitic input could produce covarying
624 δ¹³C_{carb} and %CaCO₃ records (Reuning et al., 2002), like that found in Santiurde.
625 However, given that minimum δ¹³C_{carb} values are found at %CaCO₃ maxima in Santiurde,
626 it can be concluded that the carbonate distribution does not record variations in the supply
627 of platform-derived fine-grained aragonitic and high-Mg calcite.

628 Whole rock δ¹³C and δ¹⁸O average values similar to those obtained in Santiurde were also
629 found in the coeval Rodiles hemipelagic section from the Asturian basin (Deconinck et
630 al., 2020), with that isotopic trend being considered to reveal primary environmental
631 changes. In fact, δ¹⁸O_{carb} values from Santiurde are within the average range of those
632 obtained from Pliensbachian belemnites from the Asturian basin (Gómez et al., 2016;
633 Armendáriz et al., 2012), which were used for palaeoceanographic reconstructions.
634 Taking everything into account, it can be concluded that the δ¹³C_{carb} record from
635 Santiurde may reflect the original isotopic composition of seawater, but it cannot be
636 excluded that the fluctuations respond to original variations in the isotopic signal of pore
637 waters the rate of recrystallization. However, the elemental geochemical evidence further

638 suggests that, in addition to the original composition and porosity of the different layers,
639 the Santiurde rhythmites also records variations in the supply of terrigenous components.
640 Thus, diagenetically inert trace elements, such as Ti_{EF} , also show variations in line with
641 the lithological alternations (Nohl et al., 2021).

642 Other elements, such as Sr, Fe and Mn, are sensitive to burial and may be used to assess
643 the degree of diagenetic overprinting in carbonates in combination with $\delta^{18}O_{carb}$ values
644 (Marshall, 1992; Rosales et al., 2001; Zhao and Zheng, 2014). In general, during
645 diagenesis, marine carbonates tend to become depleted in Sr and $\delta^{18}O$, but enriched in Fe
646 and Mn (Banner and Hanson, 1990). There is no correlation between the abundance of
647 these three elements in Santiurde (Fig. S5S6; Sr-Mn r: 0.03, p: 0.9; Sr-Fe r: 0.06, p: 0.82;
648 Mn-Fe r: 0.14, p: 0.58). Moreover, $\delta^{18}O_{carb}$ values do not display any correlation with Sr
649 and Mn and show positive correlation with Fe, just the opposite of what should be
650 expected from postdepositional distortion. Similarly, if when compared with the average
651 shale composition (Li and Schoonmaker, 2003), both limestones and marls from
652 Santiurde are significantly enriched in Sr (402.5 ppm), slightly enriched in Fe (32750
653 ppm), and depleted in Mn (199 ppm). Taking everything into account, a strong diagenetic
654 overprinting can be ruled out.

655 In conclusion, burial diagenesis produced depleted inorganic stable isotope values, but
656 there are no signs of strong differential diagenesis or postdepositional redistribution of
657 geochemical components in the Santiurde section. The $\delta^{13}C_{carb}$ signal was affected by
658 early diagenetic processes related to OM decay in limestones, but not to the extent of
659 obscuring the original fluctuating trend.

660 **5.2. Fluctuations in OM content** ~~Organic matter: fluctuating composition and~~ 661 ~~preservation~~

662 Detailed multiproxy analysis carried out throughout 7 limestone-marl couplets from the
663 oldest BS-BSI cast light on the origin of OM and the sedimentary factors that controlled
664 its distribution. Rosales et al. (2006) showed that BS-intervalBSIs accumulated during
665 second order sea level rises, which originated-produced the flooding of large continental
666 areas and the creation of a moderately isolated epicontinental sea, in which water
667 circulation was relatively restricted. More specifically, sluggish circulation at the
668 depocentres of the irregular floor of the BCB contributed to increasing density
669 stratification of the water-column and caused a sea floor depleted in oxygen (Wignall,
670 1991; Quesada et al., 2005), which prevented oxidation of the high organic matter content
671 of the section.

672 **5.2.1. Composition of OM**

673 ~~Previous studies demonstrated that the greatest part of the organic matter found in the~~
674 ~~BCB-Pliensbachian black shales had a marine origin, being dominated by amorphous and~~
675 ~~structured liptinitic organic matter (Suárez-Ruiz and Prado, 1987; Quesada et al., 1997,~~
676 ~~2005; Permanyer et al., 2013). The study of saturated biomarkers corroborated a dominant~~
677 ~~pattern of mature extracts derived from marine algal components. Additionally, SEM~~

678 analysis carried out in the present study provided evidence of the occurrence of biofilms
679 with sporadic occurrences of vitrinite (Fig. 3E and F).

680 The average organic C/N ratio of 30.45 obtained in Santiurde (Fig. 7) is significantly
681 higher than that of modern marine organic matter, which usually displays values between 5
682 and 18 (Meyers, 2006). However, C/N ratios observed in current reservoirs cannot be
683 directly extrapolated to ancient rocks, especially to those deposited under high
684 productivity conditions (Nijenhuis and Lange, 2000; Meyers et al., 2006; Schneider Mor
685 et al., 2012). Meyers et al. (2006) observed that organic components from Albian to
686 Santonian black shales from Demerara Rise were mainly marine in origin, but their C/N
687 ratio varied between 20 and 45, which is commonly assigned to terrestrial plants. Those
688 high C/N values were related to a more rapid recycling of N than C during OM
689 decomposition. Under oxic to anoxic conditions, modern marine organic matter is
690 commonly degraded via denitrification, decomposing principally nitrogen rich
691 aminoacids and reducing the total organic N of sediments (Altabet et al., 1995; Van Mooy
692 et al., 2002). Thus, high C/N values of some Mediterranean sapropels and Cretaceous
693 black shales have been related to the drawdown of dissolved oxygen in the water column
694 under conditions of high export productivity (Nijenhuis and Lange, 2000; Schneider Mor
695 et al., 2012). Similar processes might have controlled OM degradation in Santiurde,
696 producing the abovementioned high C/N ratio. In this regard, considering that the C/N
697 ratio of typical marine OM is closer to ~6, at least ~23% of the original N must have been
698 removed from the Santiurde deposits due to denitrification. This percentage is higher than
699 that calculated by experimentation (~9%) in recent sediments (Van Mooy et al., 2002),
700 but significantly lower than the 70% deduced from Cretaceous indurate successions
701 (Schneider Mor et al., 2012). This suggests that other processes related to OM
702 degradation, as well as the duration of the process, determine the loss of N due to
703 differential degradation.

704 The $\delta^{13}\text{C}_{\text{org}}$ signal from Santiurde is also relatively depleted if compared to modern
705 marine OM, being closer to values of terrestrial plants (Schneider Mor et al., 2012).
706 However, similarly depleted $\delta^{13}\text{C}_{\text{org}}$ values of marine OM have also been found in other
707 indurate successions (Nijenhuis and Lange, 2000; Schneider Mor et al., 2012). This
708 general depletion of $\delta^{13}\text{C}_{\text{org}}$ compared to average algal tissue is associated with selective
709 decomposition of carbohydrates and proteins enriched in $^{13}\text{C}_{\text{org}}$, which are more easily
710 decomposed, and the fortification of the lipid fraction enriched in $^{12}\text{C}_{\text{org}}$ (Jenkyns and
711 Clayton, 1986). A similar fractionation process was invoked in other sections, such as the
712 Cretaceous oil shales from Israel (Schneider Mor et al., 2012) and the Mediterranean
713 Pliocene sapropels (Nijenhuis and Lange, 2000).

714 In conclusion, poorly oxygenated background conditions of bottom waters triggered
715 denitrification of marine OM in Santiurde, promoting a selective decomposition of
716 nitrogen-rich aminoacids and the fraction enriched in $^{13}\text{C}_{\text{org}}$. This process may have been
717 stronger during the deposition of OM-rich shales.

718 **5.2.2. Fluctuations in OM content and characteristics**

719 In Santiurde, the OM content fluctuates in line with lithology, suggesting that the
720 environmental factors that controlled its accumulation and/or preservation varied
721 cyclically (Fig. 7). The fluctuations in OM content could be the result of variations in
722 either the flux of organic matter to the sea floor (i.e., fluctuations in productivity), or the
723 rate of dilution by terrestrial or carbonate sedimentary inputs, or the rate of organic-matter
724 remineralization (i.e., fluctuations in preservation) due to changing seawater oxygen
725 concentrations (Tyson, 2005; Swart et al., 2019). The greatest part of the organic matter
726 found in the BCB Pliensbachian black shales had a marine origin (see Appendix A;
727 Suárez-Ruiz and Prado, 1987; Quesada et al., 1997, 2005; Permanyer et al., 2013).

728 Many factors affect sedimentary $\delta^{13}\text{C}_{\text{org}}$ values of marine sediments, such as biological
729 sources, recycling of organic matter, and marine productivity (e.g., Nijenhuis and Lange,
730 2000; Tyson, 2005; Meyers et al., 2006; Luo et al., 2014). Changes in marine productivity
731 can be ruled out for the Santiurde $\delta^{13}\text{C}_{\text{org}}$ fluctuations. Indeed, increased OM production
732 generally results in greater sequestration of ^{12}C , which would originate lead to higher
733 $\delta^{13}\text{C}_{\text{org}}$ values when OM content increased (Meyers et al., 2006), just the opposite of the
734 Santiurde trend (Fig. 7). This is also confirmed by $\delta^{15}\text{N}_{\text{org}}$ values, which can also be
735 subject to fractionation due to variations in productivity. N is assimilated by organisms
736 in order to produce biomass, preserving the $\delta^{15}\text{N}_{\text{org}}$ value of its source. Marine $\delta^{15}\text{N}_{\text{org}}$
737 values are influenced by changes in ocean circulation, the strength of biological pump,
738 large scale N cycling, and redox conditions (Robinson et al., 2012). Nitrogen isotopes
739 have been used as a powerful tool in the analysis of petroleum systems in order to evaluate
740 unconventional reservoirs, deduce palaeoenvironmental conditions, and assess organic
741 matter sources (Quan and Adeboye, 2021). However, $\delta^{15}\text{N}_{\text{org}}$ values may also be subject
742 to alterations distortions during sedimentation, burial diagenesis, catagenesis and
743 hydrocarbon migration (Robinson et al., 2012; Quan and Adeboye, 2021). Average
744 $\delta^{15}\text{N}_{\text{org}}$ values from Santiurde (Fig. 7) are close to the current ocean isotopic ratio (~5‰;
745 Robinson et al., 2012) and vary within the range observed in other organic-rich sediments
746 and rocks (principally shales and marlstones; Holloway and Dahlgren, 2002). Increased
747 N fixation rates have been observed in modern and ancient marine records in episodes of
748 increased nutrient supply modulated by precession cycles (Higginson et al., 2003; Swart
749 et al., 2019). In such cases, low $\delta^{15}\text{N}_{\text{org}}$ values come coincide with increased primary
750 productivity and OM accumulation, just the opposite of the relationship found in
751 Santiurde. Alternatively, in other marine records, the shallow water $\delta^{15}\text{N}_{\text{org}}$ signal
752 suffered fractionation due to the liberation of bottom waterswater enriched in $^{15}\text{N}_{\text{org}}$
753 (upwelling systems; Altabet et al., 1995). In those cases, marine productivity increased
754 due the liberation of nutrients stored in the sea bottom and greater more OM with a
755 relatively higher $\delta^{15}\text{N}_{\text{org}}$ signal was produced. However, the restricted palaeogeographic
756 setting and the sedimentary features preserved (absence of phosphatic and glauconitic
757 deposits) do not support the influence of upwelling currents in Santiurde.

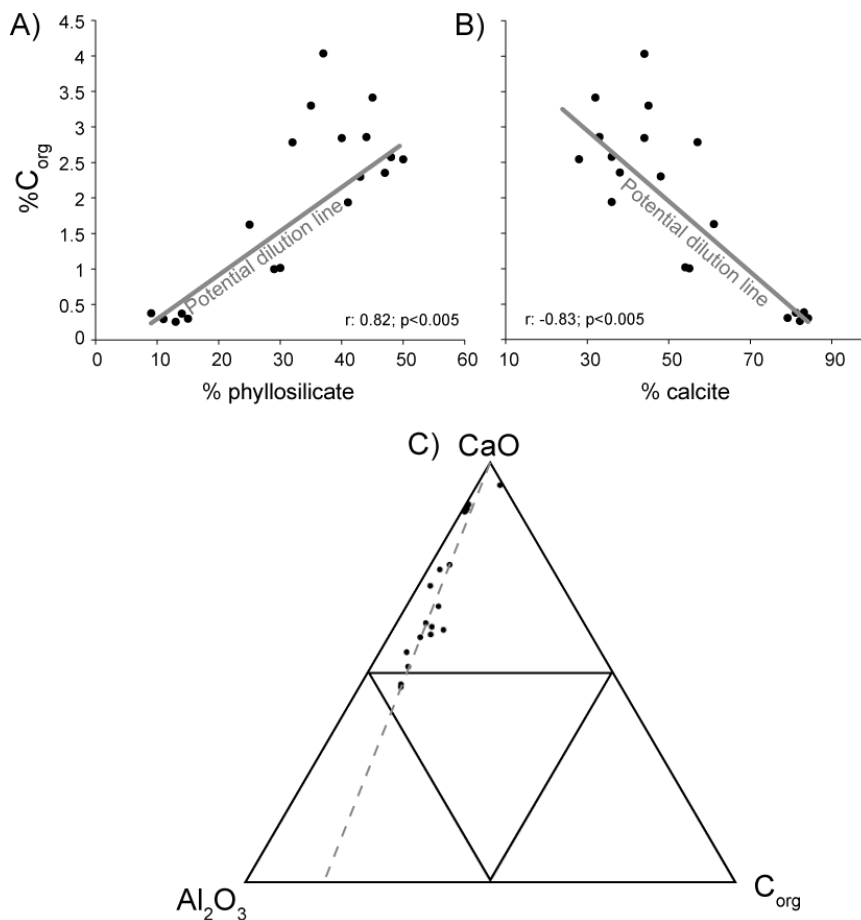
758 Average P_{EF} values from Santiurde are relatively depleted in P (Li and Schoonmaker,
759 2003), but the P content, as well as P_{EF} record in almost all couplets, displays a fluctuating
760 trend with maxima at OM-rich marls/shales (Fig. 9). Greater accumulation of P in

761 marls/shales suggests that OM might have increased due to enhanced marine productivity
762 (Calvert and Pedersen, 2007). Although Ba related indexes would not support this
763 interpretation, ~~it should be taken into account that~~ authigenic barite dissolves when
764 bottom water oxygenation is limited (Dymond et al., 1992; Tribovillard et al., 2006).
765 Consequently, it is possible that the Ba content does not reflect palaeoproductivity ratios.
766 Although P_{EF} data support a relationship between greater OM accumulation and higher
767 palaeoproductivity, ~~driven by the intensification of nutrient input~~ (Tribovillard et al.,
768 2006; Swart et al., 2019). ~~However,~~ a more comprehensive palaeoecological study
769 should be carried out in order to ~~explore whether OM fluctuations corresponded to actual~~
770 ~~variations in palaeoproductivity support this interpretation.~~

771 Fluctuations in the rate of dilution of OM by non-organic components can also result in
772 an alternation of organic-rich and organic-poor beds (Bohacs et al., 2005). In Santiurde
773 C_{org} and phyllosilicate content show a strong positive correlation ($r: 0.82; p < 0.005$; Fig.
774 12A) and covary in line with the ~~rhythmic rhythmite succession~~. This shows that C_{org}
775 oscillations were not caused by variations in the rate of dilution by clays. The CaO-Al₂O₃-
776 C_{org} ternary plot (Fig. 12C) also illustrates that the C_{org}/Al_2O_3 ratio is relatively constant,
777 whereas a higher variability is observed in the CaO/Al₂O₃ and C_{org}/CaO ratios. Therefore,
778 C_{org} fluctuations could have resulted from cyclic variations in the dilution rate by calcite
779 input. In fact, the crossplot between calcite and C_{org} shows a strong negative correlation
780 (Fig. 12B; $r: -0.83; p < 0.005$), which is typical of dilution driven OM fluctuations (Arthur
781 and Dean, 1991; Beckmann et al., 2005). In order to disentangle the origin of the cyclic
782 sedimentation, bed thickness and duration must be taken into consideration (Einsele and
783 Ricken, 1991). If variations in the rate of carbonate sedimentation had been the only
784 process controlling organic matter dilution, while OM and clay mineral inputs stayed
785 constant, limestone ~~beds~~ ~~would~~ have been significantly thicker than marls/shales, which
786 is not the case in Santiurde (Fig. 6A). This suggests that a greater input of clay minerals
787 must also have occurred during the deposition of marls/shales. ~~Moreover,~~ marls/shales
788 ~~samples with higher clay mineral content and lower calcite content~~ display greater
789 dispersion in the C_{org} vs calcite crossplot (Fig. 12B). ~~This pattern,~~ which suggests that
790 ~~when marl/shales were being deposited,~~ there might have been another factor controlling
791 OM content, such as changes in OM production or preservation, when they accumulated
792 (Bohacs et al., 2005).

793 Accordingly, the sedimentological and geochemical evidence strongly suggests that the
794 fluctuations in OM content ~~found in the Santiurde rhythmite~~ were closely related to
795 variations in the rate of organic-matter remineralization (preservation) as a consequence
796 of secular variations in seawater oxygen concentrations. ~~Thus, the characteristics of~~
797 ~~shales, such as well~~ The well-preserved lamination, the absence of burrows and the
798 scarcity of benthic fauna (Figs. 2 and 3) of shales, strongly suggest that the sea bottom
799 floor was depleted in oxygen. Conversely, bioturbation structures and benthic fauna are
800 more diverse and abundant in limestones, suggesting a better oxygenation of the seabed
801 (Figs. 2 and 3). Changing redox conditions can also be deduced from $\delta^{13}C_{org}$ records
802 (Algeo and Liu, 2020). Microbial chemoautotrophy, which is typical of oxygen-depleted

803 environments, fixes carbon enriched in ^{12}C , producing lower $\delta^{13}\text{C}_{\text{org}}$ values than OM
 804 produced by photosynthetic eukaryotic algae (Nijenhuis and Lange, 2000; Luo et al.,
 805 2014). Accordingly, minima in $\delta^{13}\text{C}_{\text{org}}$ from OM-rich marls/shales from Santiurde are
 806 very likely related to reducing deep-water conditions, similar to those deduced for some
 807 Pliocene Sapropels (Nijenhuis and Lange, 2000). The strong negative correlation between
 808 C_{org} content and $\delta^{13}\text{C}_{\text{org}}$ ($r: -0.945, p < 0.0001$) supports the close relationship between
 809 seabed oxygenation conditions and OM preservation. This interpretation is in line with
 810 that derived from the abovementioned C/N ratio (Appendix A), which also suggests that
 811 denitrification intensified during deposition of marls/shales due to more reducing sea
 812 bottom conditions.



813
 814 Figure 12. Crossplot of C_{org} against (A) phyllosilicate and (B) calcite content. Potential dilution lines of C_{org} are marked
 815 in both graphs. C) Ca-Al- C_{org} ternary plot with Santiurde samples, which follow a constant $\text{C}_{\text{org}}/\text{Al}_2\text{O}_3$.

816 The interpretations above are also supported by N_{org} and $\delta^{15}\text{N}_{\text{org}}$ data. Denitrification can
 817 result in $\delta^{15}\text{N}_{\text{org}}$ isotope fractionation in poorly oxygenated conditions, as denitrification
 818 and anaerobic ammonium oxidation reactions increase $^{15}\text{N}_{\text{org}}$ in OM (Robinson et al.,
 819 2012). In Santiurde $\delta^{15}\text{N}_{\text{org}}$ isotopes fluctuate in line with the lithological
 820 rhythmites (Fig. 7), showing maxima at marls/shales and hence a significant
 821 negative correlation with $\delta^{13}\text{C}_{\text{org}}$ ($r: -0.70, p < 0.005$) and positive correlations with C_{org} ($r:$
 822 $0.66, p < 0.005$) and N_{org} ($r: 0.73, p < 0.005$) content. **This suggests that both isotopic signals**
 823 **were probably controlled by similar environmental factors.** It can therefore be concluded

824 that $\delta^{15}\text{N}_{\text{org}}$ values increased during the accumulation of marls/shales, when bottom water
825 oxygenation decreased and denitrification intensified.

826 Pyrite and C_{org} contents also show an intermediate positive correlation in Santiurde (r:
827 0.6, $p < 0.01$). Pyrite might be formed during very early **diagenesis** due to reactions
828 between Fe and H_2S . H_2S is generally released into pore **waterswater** when sulphate-
829 reducing bacteria use sedimentary organic matter as a reducing agent and energy source
830 (Berner, 2013). More oxygenated conditions during the deposition of limestones could
831 have inhibited the formation of pyrite. Conversely, limestones present higher **magnetic**
832 **susceptibilityMS** values than marls/shales, possibly associated with a greater
833 concentration of magnetite (Fig. **S2S3**). Magnetite could be either detrital in origin or
834 related to postdepositional changes in redox state, as more oxygenated conditions favour
835 the partial replacement of pyrite with iron oxides, such as magnetite (Lin et al., 2021).

836 Finally, the correlation matrix (Table 1) and the factor analysis (Fig. 11) also show a close
837 relationship between some redox sensitive elements (Fig. 10; V, Zn, Co, Cu, Ni), pyrite
838 and C_{org} content (Calvert and Pedersen, 2007; Algeo and Liu, 2020). Enrichment factors
839 and ratios highlight a relative enrichment in redox sensitive elements throughout the
840 succession, which supports the general depositional model of a sea floor depleted in
841 oxygen (Quesada et al., 2005; Rosales et al., 2006). Trace-metal enrichment factors and
842 bielemental ratios associated with both sulphides and organic matter vary in line with the
843 lithological **rhythmicrhythmites** and support the interpretation of alternating
844 environmental redox conditions. ~~Similarly, a higher content in authigenic Barite in~~
845 ~~limestones may indicate more oxygenated conditions.~~

846 To sum up, the multiproxy analyses **$\delta^{15}\text{N}_{\text{org}}$, $\delta^{13}\text{C}_{\text{org}}$, trace elements, mineralogy and**
847 **sedimentology** shows that **the higher C_{org} content in marls/shales was related to less**
848 **oxygenated sea-bottom-floor conditions, which enhanced the preservation potential of**
849 **organic matter. The P_{EF} record suggests that the production of organic matter may also**
850 **have increased during the formation of marls/shales, but this signal is not coherent**
851 **throughout the studied interval. Given the close relationship between these processes and**
852 **the lithological rhythmites, it can be concluded that there must have been an orbitally**
853 **driven environmental factor that triggered fluctuations in bottom waterswater**
854 **oxygenation and, possibly, palaeoproductivity.**

855 **5.3. Orbitally modulated environmental changes**

856 Previous studies of North Iberian Pliensbachian records have demonstrated that this area
857 was subject to semi-arid climatic conditions, physical erosion being prevalent in the
858 continent and seawater being temperate (Rosales et al., 2004; Armendáriz et al., 2012,
859 Gómez et al., 2016; Deconinck et al., 2020). The BCB, being located close to the
860 boundary between the arid and humid climatic belts at approximately 30°N
861 palaeolatitude, was especially sensitive to orbitally driven climate change episodes, which
862 were recorded by the outer ramp hemipelagic **rhythmicrhythmites** from Santiurde. These
863 **rhythmicrhythmites** are best characterized in the stratigraphic succession by decimetre-
864 scale calcareous couplets, which represent precession cycles, and metre-scale bundles

865 linked to short eccentricity cycles. The imprint of long eccentricity cycles ~~cannot~~ can also
866 be readily identified in the field, ~~but can be~~ deduced by spectral analysis (Fig. 4).
867 ~~Based on the number of orbital cycles found in Santiurde (62 precession cycles~~
868 ~~and 13.4 short eccentricity cycles) and their average duration of 20 kyr for~~
869 ~~precession cycles and 100 kyr for short eccentric cycles, the studied succession has an~~
870 ~~estimated duration of 1.29±0.05 Ma and the BSI-1 interval of 750±30 Ma (36~~
871 ~~precession cycles and 7.8 short eccentricity cycles).~~

~~The multiproxy palaeoenvironmental analysis carried out herein showed that C_{org}~~
872 ~~production and preservation varied in line with precessional cycles and was modulated~~
873 ~~by short eccentricity cycles. Although background oxygenation of the depositional area~~
874 ~~during the BS deposition was depleted in oxygen, the astronomically driven~~
875 ~~environmental changes ultimately determined the occurrence of lower oxygen conditions~~
876 ~~at the seabed when marls/shales were being accumulated and higher oxygenation~~
877 ~~conditions during limestone accumulation.~~

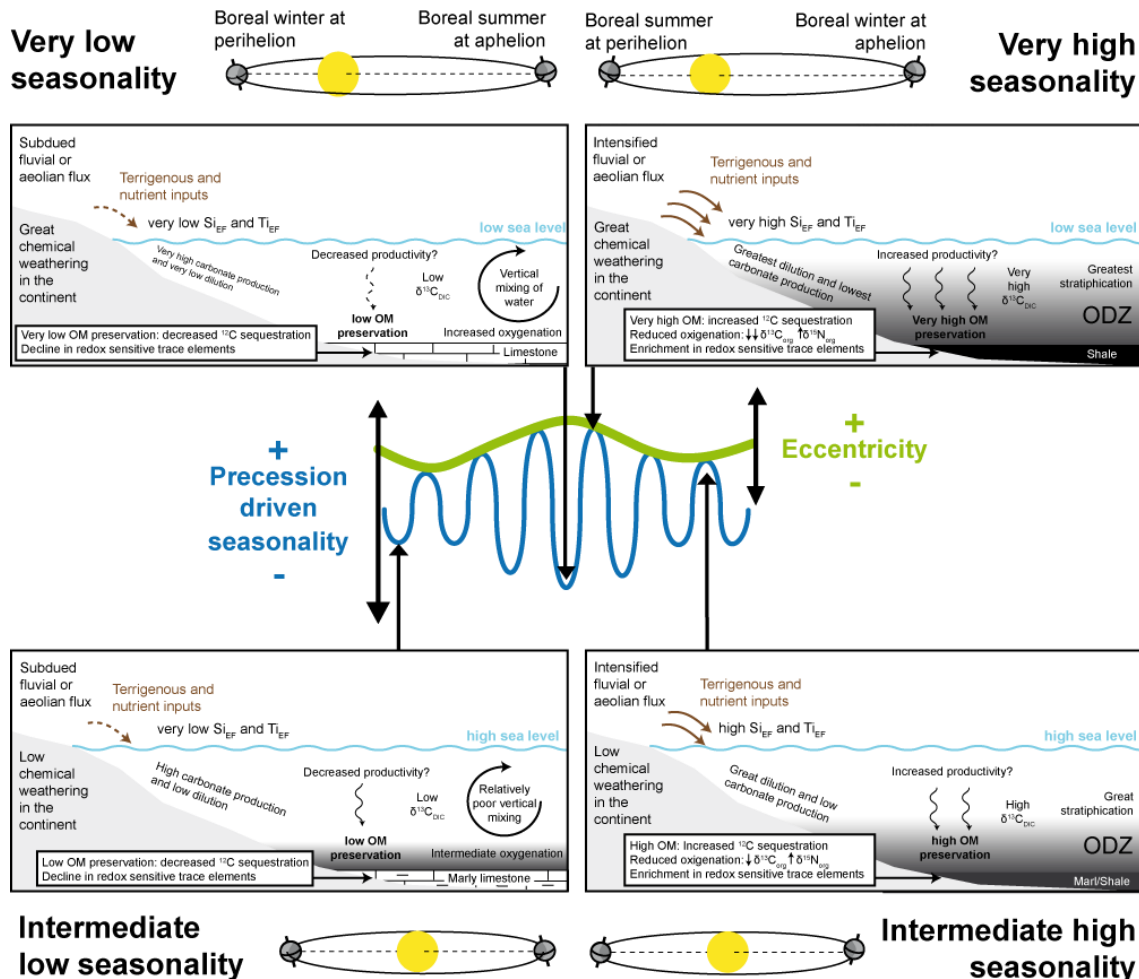
879 5.3.1. Formation of precession driven calcareous couplets

880 The sedimentary processes behind the formation of precession couplets can be analysed
881 on the basis of thickness relationships between the constituent lithologies (Einsele and
882 Ricken, 1991). When limy beds are thicker than marly beds, the formation of the
883 calcareous couplets is commonly attributed to fluctuations in either carbonate dissolution
884 or carbonate production. Contrarily, marls/shales are usually thicker than limestones
885 when periodic changes in the rate of dilution ~~of pelagic carbonate~~ by terrigenous
886 components originate the couplets. Periodic carbonate dissolution can be ruled out in
887 Santiurde, as there is neither macroscopic nor microscopic evidence of pervasive
888 carbonate dissolution and the outer carbonate ramp seabed was permanently above the
889 carbonate compensation depth (Bjerrum et al., 2001). ~~In Santiurde, the low variability of~~
890 ~~the C_{org}/Al₂O₃ ratio and the negative relationship between CaCO₃ and C_{org} indicate that~~
891 ~~fluctuations in carbonate input were an important factor in the formation of calcareous~~
892 ~~couplets. However, the~~ L/M ratio is close to 1 in most of the couplets (Fig. 6A).
893 Consequently, the formation of the Santiurde precession driven couplets most likely
894 responded to periodic changes in both carbonate production and carbonate dilution by
895 terrigenous material, increasing accumulation and preservation of C_{org} when marls/shales
896 deposited. In fact, factor analysis points out that precession driven lithological alternation
897 (Fig. 11) is strongly associated to redox sensitive variables and terrigenous proxies.

898 Given the generally semiarid Pliensbachian conditions deduced for the BCB (Dera et al.,
899 2009; Deconinck et al, 2020), a climate characterized by a prolonged dry season and a
900 short wet season can be envisaged. Dry sub-humid climates, with three to five wet months
901 per year and a maximum degree of seasonality, produce maximum values of fluvial
902 sediment discharge into the sea (Cecil and Dulong, 2003). Such high seasonality
903 conditions are generally produced when the precessional configuration results in summers
904 occurring at perihelion and winters at aphelion (Fig. 13). In Santiurde both the L/M ratio
905 and the terrigenous content of couplets suggest that shales/marls were formed in such an

906 astronomical configuration. Intensified monsoons during the wet season could have
907 increased the fluvial discharges that reached periplatform areas, producing maxima of
908 geochemical proxies associated with coarser detrital grain size, such as Si_{EF} or Ti_{EF} (Fig.
909 9; Calvert and Pedersen, 2007). However, inorganic and organic stable isotope records
910 do not support an increased input of fresh water or terrestrial OM when marls/~~and~~ shales
911 ~~were being~~ deposited. Alternatively, it is also possible that the terrigenous material was
912 transported by wind. Indeed, other studies have also related an enrichment in Si and Ti
913 content in pelagic sediments to stronger aeolian input (Rachold and Brumsack, 2001) and
914 increased dust production and transportation during high seasonality conditions
915 (Woodard et al., 2011). Thus, it can be assumed that dust generation increased in the
916 continents nearby Santiurde during ~~the~~ extremely dry seasons ~~produced~~ at precessional
917 configurations leading to maximum seasonality. Extreme seasonality conditions may also
918 have increased dust storms and dust input into the adjacent ocean (McGee et al., 2010).
919 Either aeolian or fluvial, increased terrigenous input during maximum seasonality
920 conditions may also have supplied nutrients into the ocean (P_{EF}), triggering organic
921 **phytoplankton** blooms and organic matter production. This situation promoted greater
922 OM accumulation and oxygen depletion in deep sea sediments (e.g., Nijenhuis and Lange,
923 2000; Wang, 2009; Chroustova et al., 2021). Given that the evidence of changing
924 palaeoproductivity is scarce, it is also possible that orbitally forced mechanisms also
925 modulated the amount of dissolved oxygen in seawater. As there ~~are is no evidences~~ of
926 great influence of continental water masses that could have prompted density
927 stratification of the water column (e.g., Arthur and Dean, 1991; Chroustova et al., 2021),
928 it is more likely that the mechanism was marine in origin. Interestingly, numerical
929 simulations suggested that during the Late Cretaceous hothouse both precession and
930 eccentricity cycles modulated seawater ventilation and oxygenation, driven by changes
931 in deep ocean circulation (Sarr et al., 2022). ~~According to this model, it is therefore~~
932 ~~possible that~~ basins that were depleted in oxygen, ~~like the Santiurde area,~~ were especially
933 ~~sensitive to orbitally forced ventilation variations. According to the model~~
934 ~~specifically,~~ the precessional configuration with the higher seasonality recorded the
935 greatest oxygen depletion at intermediate and deep-water **depths**, producing a strong
936 vertical oxygen gradient and seawater stratification. In Santiurde, similarly reduced
937 vertical mixing may have occurred during the accumulation of marls/shales, which would
938 have enhanced deep-water anoxia. Indeed, in Early Jurassic times, lower frequency
939 orbital cycles also triggered periodic changes in the ventilation and oxygenation of bottom
940 sediments, controlling carbonate and OM accumulation (Pieńkowski et al. 2021). Thus,
941 the southward flow of **Arctic waters** from the Boreal Sea into the Laurasian
942 epicontinental seaway favoured thermohaline circulation and the ventilation of deep
943 **waters**. However, in periods of high atmospheric CO₂, more sluggish currents or
944 stagnant conditions prevailed due to the influx of warm and saline **waters** from the
945 Tethyan area. It is possible that the early Pliensbachian BCB ~~rhythmic~~ **rhythmites** recorded
946 similar, but probably weaker, palaeoceanographic changes at precession timescales.
947 Anoxic bottom water conditions allowed OM to be preserved, favoured the precipitation
948 of authigenic sulphides and the dissolution of Fe and Mn oxo-**hydroxides** (Capet et al.,
949 2013), and altered the organic isotopic signal (enrichment in ¹³C_{org} and depletion in

950 $^{15}\text{N}_{\text{org}}$). Increased OM burial also resulted in a decrease in the ^{12}C content of inorganic
 951 carbon dissolved in seawater (Mackensen and Schmiedl, 2019). Although the $^{13}\text{C}_{\text{carb}}$
 952 signal found in Santiurde records this C storage fractionation, it is not possible to quantify
 953 the **diagenetic** imprint.



954 Figure 13. Orbitally tuned depositional model for the formation of the calcareous couplets and bundles from Santiurde.
 955 Schemes on the left represent environmental conditions during precessional stages with low annual seasonality (boreal
 956 summertime at aphelion). Schemes on the right represent environmental conditions during precessional stages with
 957 high annual seasonality stages (boreal summertime at perihelion). The influence of maximum eccentricity is shown at
 958 the top and that of minimum eccentricity at the bottom. DIC: Dissolved inorganic carbon. ODZ: Oxygen depleted zone.
 959

960 In contrast, OM-poor limy beds accumulated during low seasonality precessional stages.
 961 Such low seasonality conditions (mild summers and winters) resulted when summers
 962 occurred at aphelion and winters at perihelion (Fig. 13). Mild wet and dry seasons caused
 963 a decrease in detrital input (by wind and rivers), as well as in nutrient supply.
 964 Consequently, organic matter production and, **consequently**, bottom water oxygen
 965 consumption declined (e.g., Nijenhuis and Lange, 2000; Wang, 2009; Chroustova et al.,
 966 2021). Moreover, according to the orbitally modulated ocean circulation model (Sarr et
 967 al., 2022), low seasonality precessional stages would also have **resulted in maximum**
 968 **values of dissolved oxygen in bottom water. These environmental conditions** favoured
 969 vertical mixing of the water column, bringing oxygen to bottom **waterswater**, which
 970 allowed the oxidation stages of organic matter (Capet et al., 2013). Regarding carbonate
 971 components, previous studies have shown that Jurassic shelfal carbonate factories were

972 more efficient than pelagic ooze in micrite production (Hinnov and Park 1999; Bádenas
973 et al., 2012). It can therefore be concluded that decreased terrigenous inputs into shallow
974 marine areas further increased shelfal carbonate mud production, surpluses being
975 exported into deeper areas (Tucker et al., 2009; Bádenas et al., 2012). Assuming the
976 general $\delta^{13}\text{C}_{\text{carb}}$ trend to be primary, the enrichment in ^{12}C of limestones could correspond
977 to the OM balance in the marine environment (Mackensen and Schmiedl, 2019). Thus,
978 well oxygenated bottom waterswater allowed most of the ^{12}C -rich OM to be oxidized
979 before burial, decreasing the $\delta^{13}\text{C}$ of inorganic carbon dissolved in seawater.

980 The palaeoenvironmental model derived from the Santiurde precession couplets differs
981 significantly from those presented by others for lower Pliesbachian successions from NW
982 and central Europe (Fig. 1; Martinez and Dera, 2015; Hollar et al., 2023). However, it
983 should be taken into account that these models were developed for successions
984 accumulated in the humid climatic belt, where wet conditions prevailed throughout the
985 year and seasonality was generally weak. In such settings, terrigenous and nutrient inputs
986 increased at precessional configurations with higher seasonality, causing greater
987 productivity during the wettest season and stronger vertical water mixing during the drier
988 season. Consequently, the more calcareous OM-poor beds accumulated at high
989 seasonality precessional stages.

990 **5.3.2. Formation of eccentricity driven bundles**

991 During an eccentricity cycle, the amplitude of precession-driven seasonality cycles is
992 modulated by variations in the shape of the orbit of the Earth around the Sun (Berger and
993 Loutre, 1994). At maximum eccentricity the orbit of the Earth is elliptical and,
994 consequently, insolation changes as much as 24% in one single year, causing significantly
995 contrasting seasonality conditions. ~~In the northern hemisphere seasonality is maximized
996 when summers occur at perihelion and winters at aphelion, but seasonality is minimized
997 when winters occur at perihelion and summers at aphelion~~ (Fig. 13). On the contrary, at
998 minimum eccentricity the orbit of the Earth is almost circular, which results in relatively
999 small variations in insolation between aphelion and perihelion, regardless of the
1000 precession-driven orientation of the axis of the Earth. In short, two extreme climatic
1001 situations (maximum and minimum seasonality) alternate throughout 20 kyr precession
1002 cycles at maximum eccentricity, whereas climatic conditions remain stable for longer
1003 periods at eccentricity minima.

1004 In Santiurde the arrangement of couplets in bundles is the lithological expression of the
1005 modulation of the amplitude of precession-driven seasonality by eccentricity cycles (Fig.
1006 2B). In the interval studied in detail, couplets C36-C37 and C41-C42, located at the
1007 boundaries between bundles B8-B9 and B9-B10, show relatively little lithological
1008 contrast (mals/shales alternating with marly limestones), which suggests formation at
1009 eccentricity minima. The rest of couplets are situated in the central parts of bundles and
1010 show a marked lithological contrast (shales alternating with limestones), which suggests
1011 formation in the two extreme situations that occur during precession cycles at maximum
1012 eccentricity. This amplitude modulation is also recorded by several geochemical and

1013 mineralogical proxies, corroborating the impact of eccentricity cycles on the formation
1014 of the rhytmite.

1015 The fluctuations in some redox sensitive (C_{org} , N_{org} , trace elements, $\delta^{13}C_{org}$, Mn_{EF}) and
1016 productivity (represented by P_{EF}) proxies, some of them associated with Factor 1 in the
1017 factorial analysis (Fig. 11), display greater amplitude during eccentricity maxima. This
1018 suggests that intensified precessional seasonality at maximum eccentricity caused an
1019 increase in terrestrial sediment and nutrient input to the sea, which ultimately resulted in
1020 the intensification of OM production and oxygen consumption (e.g., Nijenhuis and Lange,
1021 2000; Wang, 2009; Chroustova et al., 2021). Precession driven variations in oceanic
1022 currents, which controlled vertical oxygen gradient and seawater stratification, also
1023 contributed to promoting bottom water anoxia in this orbital configuration (Sarr et al.,
1024 2022).

1025 ~~On the other hand, limy beds show significant variations in $CaCO_3$ content (Fig. 6), from~~
1026 ~~minimum values at bundle boundary couplets (e.g., 32.26% in C36L) to maximum values~~
1027 ~~in the middle part of the bundles (e.g., 88.98% in C35L). Limy beds in the central part of~~
1028 ~~bundle B9 also show the lowest content in terrigenous material and coarse-grained detrital~~
1029 ~~components (Figs. 6 and 9). Conversely, marls/shales show a significantly lower variation~~
1030 ~~in $CaCO_3$ content throughout eccentricity cycles (from 24.63 to 45.33% at C35M and~~
1031 ~~C38M, respectively), although marls in the central part of the bundle display maximum~~
1032 ~~values in terrigenous material and coarse-grained detrital indices. Therefore,~~ Eccentricity
1033 cycles also modulated the low seasonality precessional stages, in which carbonate
1034 accumulation was favoured (Hinnov and Park 1999; Bádenas et al., 2012).-At extremely
1035 low seasonality conditions at eccentricity maxima, continental inputs were minimal and,
1036 consequently, so was marine OM production. At the same time, oceanic currents
1037 intensified vertical mixing of water, favouring a well oxygenated water column and
1038 carbonate production (Sarr et al., 2022).

1039 Moreover, factor 2, which comprises proxies associated with dilution of carbonate by
1040 terrigenous input, show an interesting trend in line with eccentricity bundles. Scores of
1041 factor 2, in addition to fluctuating with the lithological alternation of calcareous couplets,
1042 also display a larger scale trend with minimum values at eccentricity maxima and
1043 maximum values at eccentricity minima. This trend is mainly produced by Na_2O and
1044 $^{13}C_{carb}$ (Table S5). Indeed, Na_{EF} also shows a similar trend, with generally lower values
1045 at eccentricity maxima (Fig. 9). This may record increased chemical weathering in the
1046 continent and the release of Na_2O (Marshall, 1992). This goes against the orbitally
1047 modulated climatic model of Martinez and Dera (2015), who concluded that chemical
1048 weathering increases during low seasonality and annually wet climates developed at
1049 eccentricity minima. Data from Santiurde, however, suggest that the climate was drier at
1050 eccentricity minima.

1051 5.3.3. Orbitally paced sea level changes?

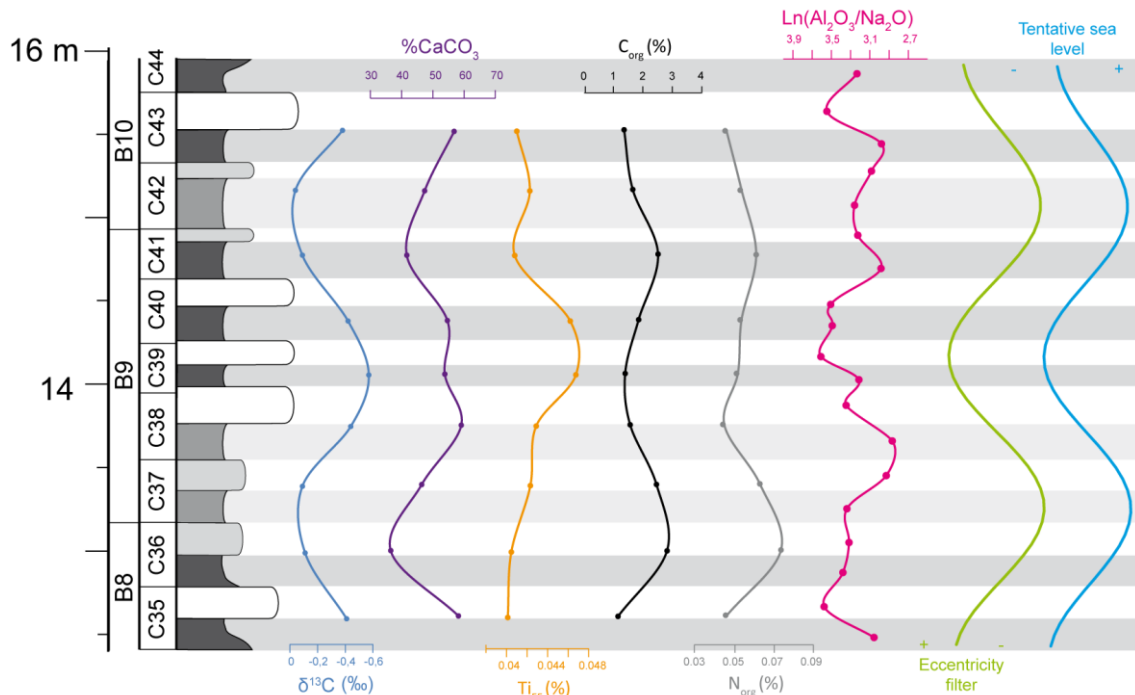
1052 It is well known that, during icehouse periods, climate change driven by high-frequency
1053 orbital cycles affects sea level due to fluctuations in the storage of water in continental

1054 ice, causing the so called glacio-eustatic sea level changes (Steffen et al., 2010). High-
1055 frequency sea level changes have also been deduced from many shallow marine platforms
1056 developed in ice-free, greenhouse periods (Haq, 2014). In the absence of extensive ice
1057 caps, sea level changes must have been caused by forcing mechanisms other than
1058 glacioeustasy, which are still debated. The thermal expansion/contraction of water masses
1059 causes sea level changes, but does not produce high amplitude variations (Conrad, 2013).
1060 Fluctuations in water storage in continental areas (principally in aquifers) seems to be a
1061 plausible forcing mechanism of decametric sea level changes during greenhouse
1062 conditions (Wendler and Wendler, 2016). According to the aquifer-eustatic model, low
1063 sea levels occur when large volumes of water are stored in the continents during humid
1064 stages, whereas sea-level rises during dry epochs due to increased aquifer discharge
1065 (Sames et al., 2020). Consequently, in a greenhouse context, orbitally driven alternations
1066 of arid and humid periods can ~~originate-produce~~ 3rd and 4th order sea level fluctuations
1067 (Wendler and Wendler, 2016; Sames et al., 2020). Greater accumulation of $\delta^{18}\text{O}$ and $\delta^{13}\text{C}$
1068 depleted fresh water in the continent results in heavier $\delta^{18}\text{O}$ and $\delta^{13}\text{C}$ of inorganic carbon
1069 dissolved in seawater, and viceversa.

1070 Second order sea level changes occurred in Early Jurassic times in the BCB, which were
1071 recorded by $\delta^{13}\text{C}$ in well preserved belemnites (Rosales et al., 2006). Highstand deposits
1072 show maximum values in OM content and $\delta^{13}\text{C}$ values in belemnites, while lowstand
1073 intervals are characterized by carbonate-rich sedimentation and lower $\delta^{13}\text{C}$ values in
1074 belemnites. These carbon-isotope records reflect fluctuations in the $\delta^{13}\text{C}$ composition of
1075 the inorganic carbon dissolved in seawater, which were controlled by periodic variations
1076 in OM burial and storage of ^{12}C in the seabed (Quesada et al., 2005; Rosales et al., 2006).
1077 This suggests that water stratification increased and ventilation of the seabed decreased
1078 in highstands. Martinez and Dera (2015) showed that $\delta^{13}\text{C}$ values from Jurassic and
1079 Lower Cretaceous perythetyan successions also recorded second and third order sea level
1080 changes modulated by orbital cycles. According to this study, flooding of continental
1081 areas at highstands triggered marine productivity and, consequently, seawater $\delta^{13}\text{C}$ values
1082 increased in neritic domains.

1083 In Santiurde, several lines of evidence suggest that short eccentricity cycles could have
1084 modulated sea level. Factor 2 scores (~~which are greatly influenced by changes in~~
1085 ~~terrigenous material and $\delta^{13}\text{C}_{\text{carb}}$; see t~~Table S5) change in line with eccentricity bundles,
1086 displaying higher values at eccentricity minima and lower values at eccentricity maxima
1087 (Fig. 14). Average $\delta^{13}\text{C}_{\text{carb}}$, % CaCO_3 and Ti_{EF} values per couplet show high values at
1088 eccentricity minima. Average C_{org} and N_{org} values per couplet also fluctuate in line with
1089 eccentricity bundles, showing maximum (or minimum) values in the intervals that
1090 correspond to low (or high) eccentricity configurations. This may indicate that the average
1091 OM content per precessional stage was higher at eccentricity minima, although shales at
1092 eccentricity maxima recorded maximum OM values. Using the ~~aquifer-~~
1093 ~~eustatic~~ ~~above~~ ~~mentioned~~ models, it can be postulated that low sea levels may have
1094 occurred during eccentricity maxima. Lowstand deposits recorded the highest and
1095 probably coarsest terrigenous inputs (Ti_{EF} ; Olde et al., 2015), but also the most calcareous

1096 sedimentation due to platform progradation. A lower sea level would have facilitated
 1097 seawater ventilation and OM degradation at eccentricity scale. However, ventilation at
 1098 maximum eccentricity decreased when precession-driven seasonality increased, which
 1099 temporarily enhanced OM production and preservation, and caused the accumulation of
 1100 shales on the seabed. Similarly, a higher sea level at eccentricity minima could have
 1101 decreased bottom water ventilation, contributing to OM preservation. These conditions
 1102 promoted OM accumulation even if terrigenous and nutrient inputs were not high when
 1103 shales deposited.



1104
 1105 Figure 14. Lithological log of the Santiurde interval studied in detail, showing the average value per couplet of $\delta^{13}\text{C}_{\text{carb}}$,
 1106 %CaCO₃, Ti_{EF}, C_{org} and N_{org}. The palaeoweathering index Ln(Al₂O₃/Na₂O) of all beds, the short eccentricity colour
 1107 filter output (Fig. 5) and a tentative sea level curve are also shown.

1108 Minima of Na_{EF} at high eccentricity lowstands (Fig. 8) suggest that the climate may have
 1109 been more humid than during low eccentricity highstands. The Ln(Al₂O₃/Na₂O) index is a
 1110 palaeoweathering index based on a statistical model of linear compositional and
 1111 weathering trends (Von Eynatten et al., 2003). This index is especially recommended for
 1112 rocks with a high percentage of biogenic carbonate (Montero-Serrano et al., 2015), such
 1113 as those from Santiurde. Ln(Al₂O₃/Na₂O) values in Santiurde show a gradual trend in line
 1114 with eccentricity bundles (Fig. 14). Maximum values, which indicate greater chemical
 1115 weathering in the continent, are recorded at eccentricity maxima. This configuration
 1116 agrees with the aquifer-eustatic sea level model, in which humid climates result in
 1117 increased fresh water storage in the continent and lower sea levels, whereas aquifers are
 1118 emptied in drier periods and sea-level rises (Wendler and Wendler, 2016). Jurassic sea
 1119 level changes deduced from shallower areas from the Iberian basin were also associated
 1120 with orbitally paced aquifer-eustatism (Sequero et al., 2017; Val et al., 2017).

1121 5.3.4. Comparison with orbital forcing during Mesozoic OAEs

1122 Four Lower Jurassic ~~BS-BSIs levels~~ occur in the BCB and the Asturian basin (Borrego et
1123 al., 1996; Rosales et al., 2006). The lower Toarcian ~~BS-BSI~~ correlates with the globally
1124 recorded early Toarcian Oceanic Anoxic Event (T-OAE; Jenkyns and Clayton, 1986;
1125 Hesselbo et al., 2000; Rosales et al., 2006), which was related to a perturbation in the
1126 Earth's climate originated by an abrupt addition of ¹²C into the carbon cycle. Many studies
1127 have previously demonstrated the influence of orbital forcing on the T-OAE in western,
1128 southern and northern Tethys areas (Huang and Hesselbo, 2014; Boulila and Hinnov,
1129 2017, Boulila et al., 2019). These studies revealed the general prevalence of 405-kyr
1130 eccentricity cycles in lower Jurassic records, along with a strong expression of both
1131 precession and obliquity cycles, although the influence of the latter only increased during
1132 the anoxic event. The palaeoenvironmental changes driven by obliquity cycles produced
1133 variations in productivity, seabed oxygenation and/or OM origin during the T-OAE (Suan
1134 et al., 2015). The shift in astronomical forcing during the T-OAE has also been linked
1135 with the lengthening of the terrestrial productivity season due to increases in global
1136 temperatures and humidity (Boulila and Hinnov, 2017; Boulila et al., 2019).

1137 In Santiurde, the influence of eccentricity and precession cycles prevailed during the
1138 formation of the Pliensbachian ~~BSI-1~~, with little or no evidence of obliquity forcing.
1139 Interestingly, however, precession cycles also modulated the palaeoenvironmental
1140 changes (continental weathering, oceanic productivity and redox conditions) that
1141 occurred during other Mesozoic OAEs associated with the release of greenhouse gases,
1142 such as the Cretaceous OAE 1a and 1b events (Giorgianni et al 2015; Benamara et al.,
1143 2020). It can therefore be concluded that the Pliensbachian ~~BSI-1~~ of the BCB shows
1144 greater similarities with Cretaceous OAEs than with the Toarcian OAE. However, it
1145 should be noted that most of the astrochronological studies of the Early Jurassic, including
1146 those focused on orbital forcing on the T-OAE, were previously focused on successions
1147 located at higher latitudes than Santiurde (Suan et al., 2015; Martinez and Dera, 2015;
1148 Boulila and Hinnov, 2017; Storm et al., 2020). It is possible that, similar to the
1149 eccentricity modulated precessional depositional model, climatic belts determined the
1150 response of the sedimentary environment to similar climatic forcings.

1151 6. Conclusions

1152 Lower Pliensbachian organic-rich calcareous ~~rhythmic~~ from the BCB are the
1153 expression of periodic environmental variations that occurred in the Milankovitch-cycle
1154 band. The cyclostratigraphic analysis of rock colour and magnetic susceptibility data
1155 series showed that calcareous couplets represent precession cycles, whereas thicker
1156 bundles record short eccentricity cycles; the effect of long-eccentricity cycles, ~~despite not~~
1157 ~~being well expressed in the field~~, was also identified.

1158 The integrated sedimentological, mineralogical and geochemical analysis of a short
1159 eccentricity bundle allowed the identification of the environmental factors that governed
1160 the formation of the ~~rhythmic~~, as well as the assessment of diagenetic
1161 overprinting. Most of the compositional parameters record primary characteristics related
1162 to the formation of the calcareous ~~rhythmic~~, but inorganic stable isotope records

1163 and the distribution of several trace elements may have been somewhat affected by
1164 diagenesis during burial. However, the results allowed the definition of an original
1165 orbitally modulated depositional model which provides new insight into the formation of
1166 lower Pliensbachian organic-rich calcareous rhythmic rhythmites.

1167 The formation of precessional calcareous couplets was regulated by variations in
1168 carbonate productivity and in dilution by terrigenous supply. Thus, organic-rich
1169 marls and shales deposited during precessional configurations which led to marked
1170 annual seasonality (boreal summer at perihelion and winter at aphelion). Increased
1171 seasonal rainfall on land and terrigenous input (by rivers or wind) to marine areas boosted
1172 organic productivity in surface waters. Increased accumulation of organic matter on
1173 the seabed eventually caused poorly oxygenated bottom waters. Deep-sea
1174 deoxygenation and seawater stratification were enhanced due to changes in ocean
1175 circulation. Conversely, limy beds were formed when seasonality was minimal (boreal
1176 winter at perihelion and summer at aphelion). The consequent decrease in terrigenous
1177 inputs favoured a greater production and basinward exportation of carbonate sediment in
1178 shallow marine areas. A lower production of OM and increased vertical seawater mixing
1179 due to changes in oceanic currents, resulted in the oxidation of organic matter in the
1180 deepest environments.

1181 In addition, several proxies support that the precessional contrast between the intensity of
1182 seasonally controlled environmental factors, such as terrigenous input and oxygenation
1183 of bottom sea-water, diminished when the Earth's orbit was circular (minimum
1184 eccentricity) and increased when it was more elliptical (maximum eccentricity). The
1185 available data further suggest that short-term sea level changes may have occurred in line
1186 with short eccentricity cycles (higher sea level at eccentricity minima), probably through
1187 orbitally modulated aquifer-eustasy.

1188 The comparison with Lower Jurassic successions from other areas suggests that
1189 palaeolatitudinal climatic belts played a significant role in the response of the
1190 environment to astronomically forced climate-change episodes.

1191 -7. Appendices

1192 Appendix A

1193 Previous studies demonstrated that the greatest part of the organic matter found in the
1194 BCB Pliensbachian black shales had a marine origin, being dominated by amorphous and
1195 structured liptinitic organic matter (Suárez-Ruiz and Prado, 1987; Quesada et al., 1997,
1196 2005; Permanyer et al., 2013). The study of saturated biomarkers corroborated a dominant
1197 pattern of mature extracts derived from marine algal components. Additionally, SEM
1198 analysis carried out in the present study provided evidence of the occurrence of biofilms
1199 with sporadic occurrences of vitrinite (Fig. 3E and F).

1200 The average organic C/N ratio of 30.45 obtained in Santiurde (Fig. 7) is significantly
1201 higher than that of modern marine organic matter, which usually displays values between

1202 5 and 18 (Meyers, 2006). However, C/N ratios observed in current reservoirs cannot be
1203 directly extrapolated to ancient rocks, especially to those deposited under high
1204 productivity conditions (Nijenhuis and Lange, 2000; Meyers et al., 2006; Schneider-Mor
1205 et al., 2012). Meyers et al. (2006) observed that organic components from Albian to
1206 Santonian black shales from Demerara Rise were mainly marine in origin, but their C/N
1207 ratio varied between 20 and 45, which is commonly assigned to terrestrial plants. Those
1208 high C/N values were related to a more rapid recycling of N than C during OM
1209 decomposition. Modern marine organic matter is commonly degraded via denitrification,
1210 decomposing principally nitrogen-rich aminoacids and reducing the total organic N of
1211 sediments (Altabet et al., 1995; Van Mooy et al., 2002). Thus, high C/N values of some
1212 Mediterranean sapropels and Cretaceous black shales have been related to the drawdown
1213 of dissolved oxygen in the water column under conditions of high export productivity
1214 (Nijenhuis and Lange, 2000; Schneider-Mor et al., 2012). Similar processes might have
1215 produced the abovementioned high C/N ratio in Santiurde,. In this regard, considering
1216 that the C/N ratio of typical marine OM is closer to ~6, at least ~23% of the original N
1217 must have been removed from the Santiurde deposits due to denitrification. This
1218 percentage is higher than that calculated by experimentation (~9%) in recent sediments
1219 (Van Mooy et al., 2002), but significantly lower than the 70% deduced from Cretaceous
1220 indurated successions (Schneider-Mor et al., 2012). This suggests that other processes
1221 related to OM degradation determine the loss of N due to differential degradation.

1222 The $\delta^{13}\text{C}_{\text{org}}$ signal from Santiurde is also relatively depleted if compared to modern
1223 marine OM, being closer to values of terrestrial plants (Schneider-Mor et al., 2012).
1224 However, similarly depleted $\delta^{13}\text{C}_{\text{org}}$ values of marine OM have also been found in other
1225 indurated successions (Nijenhuis and Lange, 2000; Schneider-Mor et al., 2012). This
1226 general depletion of $\delta^{13}\text{C}_{\text{org}}$ compared to average algal tissue is associated with selective
1227 decomposition of carbohydrates and proteins enriched in $^{13}\text{C}_{\text{org}}$, which are more easily
1228 decomposed, and the fortification of the lipid fraction enriched in $^{12}\text{C}_{\text{org}}$ (Jenkyns and
1229 Clayton, 1986). A similar fractionation process was invoked in other sections, such as the
1230 Cretaceous oil shales from Israel (Schneider-Mor et al., 2012) and the Mediterranean
1231 Pliocene sapropels (Nijenhuis and Lange, 2000).

1232 In conclusion, poorly oxygenated background conditions of bottom water triggered
1233 denitrification of marine OM in Santiurde, promoting a selective decomposition of
1234 nitrogen-rich aminoacids and the fraction enriched in $^{13}\text{C}_{\text{org}}$. This process may have been
1235 stronger during the deposition of OM-rich shales.

1236 **8. Data availability**

1237 All datasets are available open access in PANGAEA. These include magnetic susceptibility
1238 (<https://doi.pangaea.de/10.1594/PANGAEA.967720>) and colour values
1239 (<https://doi.pangaea.de/10.1594/PANGAEA.967723>) of the entire succession studied in the
1240 Santiurde section (0-22.5 m), as well as the calcium carbonate content
1241 (<https://doi.pangaea.de/10.1594/PANGAEA.967730>), elemental geochemistry
1242 (<https://doi.pangaea.de/10.1594/PANGAEA.968044>), organic geochemistry
1243 (<https://doi.pangaea.de/10.1594/PANGAEA.967947>), whole-rock mineralogy

1244 <https://doi.pangaea.de/10.1594/PANGAEA.967852>), and inorganic C and O isotopes
1245 <https://doi.pangaea.de/10.1594/PANGAEA.967761>) of the interval studied in detail (12.4-15.95
1246 m).

1247 **9. Author contributions.**

1248 NMB: conceptualization, formal analysis, investigation, methodology, and writing
1249 (original draft preparation). AP: conceptualization, funding acquisition, formal analysis,
1250 investigation, methodology, and writing (review and editing). JDT: formal analysis,
1251 investigation, methodology, and writing (review and editing). IR: formal analysis,
1252 investigation, and writing (review and editing). JA: formal analysis, investigation, and
1253 methodology. RSC: formal analysis and investigation.

1254 **10. Competing interests**

1255 The contact author has declared that none of the authors has any competing interests

1256 **11. Financial support**

1257 Research funded by projects PID2019-105670GB-I00/AEI/10.13039/501100011033 of
1258 the Spanish Government (MCIN/AEI) and by the Consolidated Research Group IT602-
1259 22 of the Basque Government. NM-B is grateful for post-doctoral specialization grants
1260 DOCREC19/35 and ESPDOC21/49 from the University of the Basque Country
1261 (UPV/EHU) and a Margarita Salas contract (MARSA22/05) of the Spanish Government
1262 with Next Generation funds from the European Union.

1263 **12. Acknowledgements**

1264 Research funded by projects PID2019-105670GB-I00/AEI/10.13039/501100011033 of
1265 the Spanish Government (MCIN/AEI) and by the Consolidated Research Group IT602-
1266 22 of the Basque Government. NM-B is grateful for post-doctoral specialization grants
1267 DOCREC19/35 and ESPDOC21/49 from the University of the Basque Country
1268 (UPV/EHU) and a Margarita Salas contract (MARSA22/05) of the Spanish Government
1269 with Next Generation funds from the European Union. Thanks are due to Carl Sheaver
1270 for his language corrections. This article benefited from insightful comments on a
1271 previous version of the manuscript by editor Gerilyn (Lynn) Soreghan and reviewers
1272 Beatriz Bádenas and Sietske Batenburg.

1273 **13. References**

1274 Algeo, T. J. and Liu, J.: A re-assessment of elemental proxies for paleoredox analysis,
1275 Chem. Geol., 540, 119549, <https://doi.org/10.1016/j.chemgeo.2020.119549>; 2020.

1276 Altabet, M. A., Francois, R., Murray, D. W. and Prell, W. L.: Climate-related variations
1277 in denitrification in the Arabian Sea from sediment $^{15}\text{N}/^{14}\text{N}$ ratios, Nature, 373(6514),
1278 506-509, <https://doi.org/10.1038/373506a0>, 1995.

- 1279 Aristilde, L., Xu, Y. and Morel, F. M.: Weak organic ligands enhance zinc uptake in
1280 marine phytoplankton, *Environ. Sci. & technol.*, 46(10), 5438-5445,
1281 <https://doi.org/10.1021/es300335u>, 2012.
- 1282 Armendáriz, M., Rosales, I., Bádenas, B., Aurell, M., García-Ramos, J. C. and Piñuela,
1283 L.: High-resolution chemostratigraphic records from Lower Pliensbachian belemnites:
1284 Palaeoclimatic perturbations, organic facies and water mass exchange (Asturian basin,
1285 northern Spain), *Palaeogeogr. Palaeoclimatol. Palaeoecol.*, 333, 178-191,
1286 <https://doi.org/10.1016/j.palaeo.2012.03.029>, 2012.
- 1287 Arthur, M. A. and Dean, W. E.: A holistic geochemical approach to cyclomania: examples
1288 from Cretaceous pelagic limestone sequences, in: *Cycles and events in stratigraphy*,
1289 edited by: Einsele, E., Ricken, W. and Seilacher A., Springer -Verlag, New York, 126-
1290 166, ISBN 0-387-52784-2, 1991.
- 1291 Aurell, M., Meléndez, G., Olóriz, F., Bádenas, B., Caracuel, J., García-Ramos, J.C., Goy,
1292 A., Linares, A., Quesada, S., Robles, S., Rodríguez-Tovar, F.J., Rosales, I., Sandoval, J.,
1293 Suárez de Centi, C., Tavera, J.M., and Valenzuela, M.: Jurassic, in: *The Geology of Spain*,
1294 edited by Gibbons, W., and Moreno, M.T, The Geological Society, London, 213-253,
1295 <https://doi.org/10.1144/GOSPP.11>, 2002.
- 1296 Bádenas, B., Aurell, M., Armendáriz, M., Rosales, I., García-Ramos, J. C. and Piñuela,
1297 L.: Sedimentary and chemostratigraphic record of climatic cycles in Lower Pliensbachian
1298 marl–limestone platform successions of Asturias (North Spain), *Sediment. Geol.*, 281,
1299 119-138, <https://doi.org/10.1016/j.sedgeo.2012.08.010>, 2012.
- 1300 Banner, J. L. and Hanson, G. N.: Calculation of simultaneous isotopic and trace element
1301 variations during water-rock interaction with applications to carbonate diagenesis,
1302 *Geochim. Cosmochim. Acta*, 54(11), 3123-3137, [https://doi.org/10.1016/0016-](https://doi.org/10.1016/0016-7037(90)90128-8)
1303 [7037\(90\)90128-8](https://doi.org/10.1016/0016-7037(90)90128-8), 1990.
- 1304 Bayon, G., German, C. R., Burton, K. W., Nesbitt, R. W. and Rogers, N.: Sedimentary
1305 Fe–Mn oxyhydroxides as paleoceanographic archives and the role of aeolian flux in
1306 regulating oceanic dissolved REE, *Earth Planet. Sci. Lett.*, 224(3-4), 477-4,
1307 <https://doi.org/10.1016/j.epsl.2004.05.033>; 2004.
- 1308 Beckmann, B., Wagner, T. and Hofmann, P.: Linking Coniacian–Santonian (OAE3)
1309 black-shale deposition to African climate variability: A reference section from the eastern
1310 tropical Atlantic at orbital time scales (ODP Site 959, off Ivory Coast and Ghana), in:
1311 *Deposition of Organic-Carbon-Rich Sediments: Models, Mechanisms, and*
1312 *Consequences*, edited by: Harris, N.B., Society for Sedimentary Geology (SEPM-SSG),
1313 Special Publication, 82, 125-143, <https://doi.org/10.29/2001PA00073>, 2005
- 1314 Benamara, A., Charbonnier, G., Adatte, T., Spangenberg, J. E. and Föllmi, K. B.:
1315 Precession-driven monsoonal activity controlled the development of the early Albian
1316 Paquier oceanic anoxic event (OAE1b): Evidence from the Vocontian Basin, SE France,

- 1317 Palaeogeogr. Palaeoclimatol. Palaeoecol., 537, 109406,
1318 <https://doi.org/10.1016/j.palaeo.2019.109406>, 2020.
- 1319 Berger, A., and Loutre, M.F.: Precession, eccentricity, obliquity, insolation and
1320 paleoclimates, in: Long-term Climatic Variations, NATO ASI Series, edited by Duplessy,
1321 J.C. and Spyridakis, M.T., Springer, Berlin, 22, 107–151, https://doi.org/10.1007/978-3-642-79066-9_5, 1994.
- 1323 Berner, Z. A., Puchelt, H., Noeltner, T. and Kramar, U. T. Z.: Pyrite geochemistry in the
1324 Toarcian Posidonia Shale of south-west Germany: Evidence for contrasting trace-element
1325 patterns of diagenetic and syngenetic pyrites, *Sedimentology*, 60(2), 548-573, doi:
1326 10.1111/j.1365-3091.2012.01350.x, 2013.
- 1327 Bohacs, K.M., Grabowski, G.J., Carroll, A.R., Mankiewicz, P.J., Miskell, K.J. and
1328 Schwalbach, J.R.: Production, destruction, and dilution—the many paths to source-rock
1329 development, in: *Deposition of Organic-Carbon-Rich Sediments: Models, Mechanisms,*
1330 *and Consequences*, edited by: Harris, N.B., Society for Sedimentary Geology (SEPM-
1331 SSG), Special Publication, 82, 61-101, <https://doi.org/10.2110/pec.05.82.0061>, 2005.
- 1332 Borrego, A. G., Hagemann, H. W., Blanco, C. G., Valenzuela, M. and De Centi, C. S.:
1333 The Pliensbachian (Early Jurassic) “anoxic” event in Asturias, northern Spain: Santa
1334 Mera Member, Rodiles Formation, *Org. Geochem.*, 25(5-7), 295-309,
1335 [https://doi.org/10.1016/S0146-6380\(96\)00121-0](https://doi.org/10.1016/S0146-6380(96)00121-0), 1996.
- 1336 Bougeault, C., Pellenard, P., Deconinck, J. F., Hesselbo, S. P., Dommergues, J. L.,
1337 Bruneau, L., Cocquerez, T., Laffont, R., Huret, E. and Thibault, N.: Climatic and
1338 palaeoceanographic changes during the Pliensbachian (Early Jurassic) inferred from clay
1339 mineralogy and stable isotope (CO) geochemistry (NW Europe), *Glob. Planet. Change.*,
1340 149, 139-152, <https://doi.org/10.1016/j.gloplacha.2017.01.005>, 2017.
- 1341 Boulila, S. and Hinnov, L. A.: A review of tempo and scale of the early Jurassic Toarcian
1342 OAE: implications for carbon cycle and sea level variations, *Newsl. Stratigr.*, 50(4), 363-
1343 389, DOI: 10.1127/nos/2017/0374, 2017.
- 1344 Boulila, S., Galbrun, B., Sadki, D., Gardin, S. and Bartolini, A.: Constraints on the
1345 duration of the early Toarcian T-OAE and evidence for carbon-reservoir change from the
1346 High Atlas (Morocco), *Glob. Planet. Change.*, 175, 113-128,
1347 <https://doi.org/10.1016/j.gloplacha.2019.02.005>, 2019.
- 1348 Braga, J.C., Comas-Rengifo, M.J., Goy, A., Rivas, P. and Yébenes, A.: El Lías inferior y
1349 medio en la zona central de la Cuenca Vasco-Cantábrica (Camino, Santander), in: III
1350 Coloquio de Estratigrafía y Paleogeografía del Jurásico de España, Logroño, Spain, 10-
1351 19 september 1988, Instituto de Estudios Riojanos, Ciencias de la Tierra, Geología, 11,
1352 17-45, ISBN 84-00-06877-7, 1988.
- 1353 ~~Bougeault, C., Pellenard, P., Deconinck, J. F., Hesselbo, S. P., Dommergues, J. L.,~~
1354 ~~Bruneau, L., Cocquerez, T., Laffont, R., Huret, E. and Thibault, N.: Climatic and~~
1355 ~~palaeoceanographic changes during the Pliensbachian (Early Jurassic) inferred from clay~~

- 1356 ~~mineralogy and stable isotope (CO) geochemistry (NW Europe), *Glob. Planet. Change.*,~~
1357 ~~149, 139–152, <https://doi.org/10.1016/j.gloplacha.2017.01.005>, 2017.~~
- 1358 Calvert, S.E. and Pedersen, T.F.: Elemental proxies for palaeoclimatic and
1359 palaeoceanographic variability in marine sediments: interpretations and applications, in:
1360 Proxies in Late Cenozoic Paleooceanography, edited by: Hillaire-Marcel, C. and De
1361 Vernal, A., *Developments in Marine Geology Vol. 1*, Elsevier, Oxford, UK, 567–644,
1362 [https://doi.org/10.1016/S1572-5480\(07\)01019-6](https://doi.org/10.1016/S1572-5480(07)01019-6), 2007.
- 1363 Capet, A., Beckers, J.-M., and Grégoire, M.: Drivers, mechanisms and long-term
1364 variability of seasonal hypoxia on the Black Sea northwestern shelf – is there any
1365 recovery after eutrophication?, *Biogeosciences*, 10, 3943–3962,
1366 <https://doi.org/10.5194/bg-10-3943-2013>, 2013.
- 1367 Cecil, C.B. and Dulong, F.B.: Precipitation models for sediment supply in warm climates.
1368 In: *Climate Controls on Stratigraphy*, edited by: Cecil C.B. and Edgar N.T., *SEPM Spec.*
1369 *Publ.*, 77, 21–27, <https://doi.org/10.2110/pec.03.77.0021>, 2003.
- 1370 Charbonnier, G., Boulila, S., Galbrun, B., Laskar, J., Gardin, S. and Rouget, I.: A 20-
1371 million-year Early Jurassic cyclostratigraphic record and its implications for the chaotic
1372 inner Solar System and sea-level changes, *Basin Res.*, 1288-1307,
1373 <https://doi.org/10.1111/bre.12754>, 2023.
- 1374 Chroustová, M., Holcová, K., Laurin, J., Uličný, D., Hradecká, L., Hrnková, M., Čech, S.,
1375 Hrouda, F. and Jarvis, I.: Response of foraminiferal assemblages to precession-paced
1376 environmental variation in a mid-latitude seaway: Late Turonian greenhouse of Central
1377 Europe, *Mar. Micropaleontol.*, 167, 102025,
1378 <https://doi.org/10.1016/j.marmicro.2021.102025>, 2021.
- 1379 Conrad, C. P.: The solid Earth's influence on sea level. *Geol. Soc. Am. Bull.*, 125(7-8),
1380 1027-1052, <https://doi.org/10.1130/B30764.1>, 2013.
- 1381 Cramer, B. D. and Jarvis, I.: Carbon isotope stratigraphy, In: *Geologic time scale 2020*,
1382 edited by: Gradstein, F.M., Ogg, J., Schmitz, M. and Ogg, G.M, Elsevier, Oxford, UK,
1383 309-343, <https://doi.org/10.1016/B978-0-12-824360-2.00011-5>, 2020
- 1384 Deconinck, J. F., Gómez, J. J., Baudin, F., Biscay, H., Bruneau, L., Cocquerez, T.,
1385 Mathieu, O., Pellenard, P. and Santoni, A. L.: Diagenetic and environmental control of
1386 the clay mineralogy, organic matter and stable isotopes (C, O) of Jurassic (Pliensbachian-
1387 lowermost Toarcian) sediments of the Rodiles section (Asturian Basin, Northern Spain),
1388 *Mar. Pet. Geol.*, 115, 104286, <https://doi.org/10.1016/j.marpetgeo.2020.104286>, 2020.
- 1389 Dera, G., Pellenard, P., Neige, P., Deconinck, J.-F., Pucéat, E. and Dommergues, J.-L.:
1390 Distribution of clay minerals in Early Jurassic Peritethyan seas: palaeoclimatic
1391 significance inferred from multiproxy comparisons, *Palaeogeogr. Palaeoclimatol.*
1392 *Palaeoecol.*, 271, 39–51, <https://doi.org/10.1016/j.palaeo.2008.09.010>, 2009.

- 1393 Dickson, J.A.D., Wood, R.A., Al Rougga, H.B. and Shebl, H.: Sulphate reduction
1394 associated with hardgrounds: Lithification afterburn!, *Sed. Geol.*, 205, 34–39,
1395 <https://doi.org/10.1016/j.sedgeo.2008.01.005>, 2008.
- 1396 Dinarès-Turell, J., Martínez-Braceras, N. and Payros, A.: High-Resolution Integrated
1397 Cyclostratigraphy From the Oyambre Section (Cantabria, N Iberian Peninsula):
1398 Constraints for Orbital Tuning and Correlation of Middle Eocene Atlantic Deep-Sea
1399 Records, *Geochem. Geophys.*, 19(3), 787-806, <https://doi.org/10.1002/2017GC007367>,
1400 2018.
- 1401 Dymond, J., Suess, E. and Lyle, M.: Barium in deep-sea sediment: A geochemical proxy
1402 for paleoproductivity, *Paleoceanography*, 7(2), 163-181,
1403 <https://doi.org/10.1029/92PA00181>, 1992.
- 1404 Einsele, G. and Ricken, W.: Limestone-marl alternation-an overview. Cycles and events
1405 in stratigraphy, in: *Cycles and events in stratigraphy*, edited by: Einsele, E., Ricken, W.
1406 and Seilacher A., Springer -Verlag, New York, 23-47, ISBN 0-387-52784-2, 1991.
- 1407 [Fraguas, A., Comas-Rengifo, M. J. and Perillo, N.: Calcareous nannofossil](https://doi.org/10.1127/nos/2015/0059)
1408 [biostratigraphy of the Lower Jurassic in the Cantabrian Range \(Northern Spain\).](https://doi.org/10.1127/nos/2015/0059)
1409 [Newslett. Stratig., 48\(2\), 179-199, <https://doi.org/10.1127/nos/2015/0059>, 2015.](https://doi.org/10.1127/nos/2015/0059)
- 1410 Giorgioni, M., Keller, C. E., Weissert, H., Hochuli, P. A. and Bernasconi, S. M.: Black
1411 shales—from coolhouse to greenhouse (early Aptian), *Cretac. Res.*, 56, 716-731,
1412 <https://doi.org/10.1016/j.cretres.2014.12.003>, 2015.
- 1413 Gómez, J. J., Comas-Rengifo, M. J., and Goy, A.: Palaeoclimatic oscillations in the
1414 Pliensbachian (Early Jurassic) of the Asturian Basin (Northern Spain), *Clim. Past*, 12,
1415 1199–1214, <https://doi.org/10.5194/cp-12-1199-2016>, 2016.
- 1416 Grossman, E. L. and Joachimski, M. M.: Oxygen isotope stratigraphy, in: *Geologic Time*
1417 *Scale 2020*, edited by: Gradstein, F.M., Ogg, J., Schmitz, M. and Ogg, G.M, Elsevier,
1418 Oxford, UK, 279-307, <https://doi.org/10.1016/B978-0-12-824360-2.00010-3>, 2020.
- 1419 Hallam, A.: Origin of minor limestone-shale cycles – climatically induced or diagenetic,
1420 *Geology*, 14, 609–612, <https://doi.org/10.1130/0091-7613>, 1986.
- 1421 Haq, B. U.: Cretaceous eustasy revisited, *Global and Planet. change*, 113,
1422 <https://doi.org/10.1016/j.gloplacha.2013.12.007>, 44-58.
- 1423 [Henrich, R. and Hüneke, H.: Hemipelagic advection and periplatform sedimentation.](https://doi.org/10.1016/B978-0-444-53000-4.00005-6)
1424 [Developments in sedimentology, 63, 353-396, \[https://doi.org/10.1016/B978-0-444-\]\(https://doi.org/10.1016/B978-0-444-53000-4.00005-6\)
1425 \[53000-4.00005-6\]\(https://doi.org/10.1016/B978-0-444-53000-4.00005-6\), 2011.](https://doi.org/10.1016/B978-0-444-53000-4.00005-6)
- 1426 Higginson, M. J., Maxwell, J. R. and Altabet, M. A.: Nitrogen isotope and chlorin
1427 paleoproductivity records from the Northern South China Sea: remote vs. local forcing of
1428 millennial-and orbital-scale variability, *Mar. Geol.*, 201(1-3), 223-250,
1429 [https://doi.org/10.1016/S0025-3227\(03\)00218-4](https://doi.org/10.1016/S0025-3227(03)00218-4), 2003.

- 1430 Hinnov, L.A.: Cyclostratigraphy and its revolutionizing applications in the earth and
1431 planetary sciences, *Geol. Soc. Am. Bull.*, 125(11-12), 1703–1734,
1432 <https://doi.org/10.1130/B30934.1>, 2013.
- 1433 Hinnov, L.A. and Park, J.J.: Strategies for assessing Early-Middle (Pliensbachian-
1434 Aalenian) Jurassic cyclochronologies, *Philos. Trans. R. Soc. Lond. A.*, 357,1831–1859.
1435 <https://doi.org/10.1098/rsta.1999.0403>, 1999.
- 1436 Hollaar, T. P., Hesselbo, S. P., Deconinck, J.-F., Damaschke, M., Ullmann, C. V., Jiang,
1437 M., and Belcher, C. M.: Environmental changes during the onset of the Late
1438 Pliensbachian Event (Early Jurassic) in the Cardigan Bay Basin, Wales, *Clim. Past*, 19,
1439 979–997, <https://doi.org/10.5194/cp-19-979-2023>, 2023.
- 1440 Holloway, J. M. and Dahlgren, R. A.: Nitrogen in rock: occurrences and biogeochemical
1441 implications, *Global biogeochem. cycles*, 16(4), 65-1,
1442 <https://doi.org/10.1029/2002GB001862>, 2002.
- 1443 Huang, C. and Hesselbo, S. P.: Pacing of the Toarcian Oceanic Anoxic Event (Early
1444 Jurassic) from astronomical correlation of marine sections, *Gondwana Res.*, 25(4), 1348-
1445 1356, <https://doi.org/10.1016/j.gr.2013.06.023>, 2014.
- 1446 Hüsing, S. K., Beniést, A., van der Boon, A., Abels, H. A., Deenen, M. H. L., Ruhl, M.
1447 and Krijgsman, W.: Astronomically-calibrated magnetostratigraphy of the Lower
1448 Jurassic marine successions at St. Audrie's Bay and East Quantoxhead (Hettangian–
1449 Sinemurian; Somerset, UK), *Palaeogeogr. Palaeoclimatol. Palaeoecol.*, 403, 43-56,
1450 <https://doi.org/10.1016/j.palaeo.2014.03.022>, 2014.
- 1451 Ikeda, M., Bôle, M. and Baumgartner, P. O.: Orbital-scale changes in redox condition and
1452 biogenic silica/detrital fluxes of the Middle Jurassic Radiolarite in Tethys (Sogno,
1453 Lombardy, N-Italy): Possible link with glaciation?, *Palaeogeogr. Palaeoclimatol.*
1454 *Palaeoecol.*, 457, 247-257, <https://doi.org/10.1016/j.palaeo.2016.06.009>, 2016.
- 1455 Jenkyns, H. C. and Clayton, C. J.: Black shales and carbon isotopes in pelagic sediments
1456 from the Tethyan Lower Jurassic, *Sedimentology*, 33(1), 87-106,
1457 <https://doi.org/10.1111/j.1365-3091.1986.tb00746.x>, 1986.
- 1458 Jones, B. and Manning, D. A.: Comparison of geochemical indices used for the
1459 interpretation of palaeoredox conditions in ancient mudstones, *Chem. Geol.*, 111(1-4),
1460 111-129, [https://doi.org/10.1016/0009-2541\(94\)90085-X](https://doi.org/10.1016/0009-2541(94)90085-X), 1994.
- 1461 Lewan, M. D.: Factors controlling the proportionality of vanadium to nickel in crude oils,
1462 *Geochim. Cosmochim. Acta*, 48(11), 2231-2238, [https://doi.org/10.1016/0016-7037\(84\)90219-9](https://doi.org/10.1016/0016-7037(84)90219-9), 1984.
- 1464 Li, M., Hinnov, L. and Kump, L.: Acycle: Time-series analysis software for paleoclimate
1465 research and education, *Comput. and Geosci.*, 127, 12-22,
1466 <https://doi.org/10.1016/j.cageo.2019.02.011>, 2019.

- 1467 Li, Y. H. and Schoonmaker, J. E.: Chemical composition and mineralogy of marine
1468 sediments, in: *Treatise on Geochemistry*, edited by: Holland, H.D. and Turekian, K.K.,
1469 Elsevier, Oxford, UK, 1-35, ISBN: 0-08-044342-7, 2003.
- 1470 Lin, Z., Sun, X., Roberts, A.P., Strauss, H., Lu, Y., Yang, X., Gong, J., Li, G., Brunner,
1471 B. and Peckmann, J.: A novel authigenic magnetite source for sedimentary magnetization,
1472 *Geology*, 49 (4), 360–365, <https://doi.org/10.1130/G48069.1>, 2021.
- 1473 Luo, G., Algeo, T.J., Huang, J., Zhou, W., Wang, Y., Yang, H., Richoz, S. and Xie, S.:
1474 Vertical $\delta^{13}\text{C}_{\text{org}}$ gradients record changes in planktonic microbial community composition
1475 during the end-Permian mass extinction, *Palaeogeogr. Palaeoclimatol. Palaeoecol.*, 396,
1476 119-131, <http://dx.doi.org/10.1016/j.palaeo.2014.01.006>, 2014.
- 1477 Mackensen, A. and Schmiedl, G.: Stable carbon isotopes in paleoceanography:
1478 atmosphere, oceans, and sediments, *Earth Sci. Rev.*, 197, 102893,
1479 <https://doi.org/10.1016/j.earscirev.2019.102893>, 2019.
- 1480 Mann, M. E. and Lees, J. M.: Robust estimation of background noise and signal detection
1481 in climatic time series, *Climatic change*, 33(3), 409-445,
1482 <https://doi.org/10.1007/BF00142586>, 1996.
- 1483 Marshall, J.: Climatic and oceanographic isotopic signals from the carbonate rock record
1484 and their preservation, *Geol. Mag.*, 129, 143–160,
1485 <https://doi.org/10.1017/S0016756800008244>, 1992.
- 1486 Martinez, M. and Dera, G.: Orbital pacing of carbon fluxes by a ~9-My eccentricity cycle
1487 during the Mesozoic, *P. Natl. Acad. Sci. USA*, 112, 12604–12609,
1488 <https://doi.org/10.1073/pnas.1419946112>, 2015.
- 1489 Martínez-Braceras, N., Franceschetti, G., Payros, A., Monechi, S. and Dinarès Turell, J.:
1490 High-resolution cyclochronology of the lowermost Ypresian Arnakatxa section (Basque-
1491 Cantabrian Basin, western Pyrenees), *Newsl. Stratigr.*, 54, 53-74, DOI:
1492 10.1127/nos/2022/0706, 2023.
- 1493 Martínez-Braceras, N., Payros, A., Miniati, F., Arostegi, J. and Franceschetti,
1494 G.: Contrasting environmental effects of astronomically driven climate change on three
1495 Eocene hemipelagic successions from the Basque–Cantabrian Basin, *Sedimentology*,
1496 64(4), <https://doi.org/10.1111/sed.12334>; 960-986, 2017
- 1497 McGee, D., Broecker, W. S. and Winckler, G.: Gustiness: The driver of glacial dustiness?,
1498 *Quat. Sci. Rev.*, 29, 2340–2350, doi:10.1016/j.quascirev.2010.06.009, 2010.
- 1499 Meyers, P. A.: Paleoceanographic and paleoclimatic similarities between Mediterranean
1500 sapropels and Cretaceous black shales, *Palaeogeogr. Palaeoclimatol. Palaeoecol.*, 235(1-
1501 3), 305-320, <https://doi.org/10.1016/j.palaeo.2005.10.025>, 2006.
- 1502 Meyers, S. R.: Astrochron: An R Package for Astrochronology, available at:
1503 <https://CRAN.R-project.org/package=astrochron>, 2014.

- 1504 Meyers, S.R., Sageman, B.B. and Hinnov, L.A.: Integrated quantitative stratigraphy of
 1505 the Cenomanian–Turonian bridge Creek Limestone member using evolutive harmonic
 1506 analysis and stratigraphic modelling, *J. Sediment. Res.*, 71, 628–644,
 1507 <https://doi.org/10.1306/012401710628>, 2001.
 1508
- 1509 Nijenhuis, I. A. and de Lange, G. J.: Geochemical constraints on Pliocene sapropel
 1510 formation in the eastern Mediterranean, *Mar. Geol.*, 163, 41-63,
 1511 [https://doi.org/10.1016/S0025-3227\(99\)00093-6](https://doi.org/10.1016/S0025-3227(99)00093-6); 2000.
 1512
- 1513 Nohl, T., Steinbauer, M. J., Sinnesael, M. and Jarochovska, E.: Detecting initial aragonite
 1514 and calcite variations in limestone–marl alternations, *Sedimentology*, 68(7), 3102-3115,
 1515 <https://doi.org/10.1111/sed.12885>; 2021.
- 1516 Olde, K., Jarvis, I., Uličný, D., Pearce, M.A., Trabucho-Alexandre, J., Čech, S., Gröcke,
 1517 D.R., Laurin, J., Švábenická, L. and Tocher, B.A.: Geochemical and palynological sea-
 1518 level proxies in hemipelagic sediments: a critical assessment from the Upper Cretaceous
 1519 of the Czech Republic, *Palaeogeogr. Palaeoclimatol. Palaeoecol.*, 435, 222-243,
 1520 <https://doi.org/10.1016/j.palaeo.2015.06.018>, 2015.
 1521
- 1522 Osete, M. L., Gómez, J. J., Pavón-Carrasco, F. J., Villalaín, J. J., Palencia-Ortas, A., Ruiz-
 1523 Martínez, V. C., Heller, F.: The evolution of Iberia during the Jurassic from
 1524 palaeomagnetic data, *Tectonophysics*, 502(1-2), 105-120, 2011.
 1525
- 1526 Pettijohn, F. J. (Ed.): *Sedimentary Rocks* (2nd ed.), Harper and Brothers, New York, 718
 1527 pp., ISBN 10:0060451904, 1957.
 1528
- 1529 Pieńkowski, G., Schudack, M.E., Bosák, P., Enay, R., Feldman-Olszewska, A., Golonka,
 1530 J., Gutowski, J., Hengreen, G.F.W., Jordan, P., Krobicki, M., Lathuiliere, B., Leinfelder,
 1531 R.R., Michalík, J., M'onnig, E., Noe-Nygaard, N., Pálffy, J., Pint, A., Rasser, M.W.,
 1532 Reisdorf, A.G., Schmid, D.U., Schweigert, G., Surlyk, F., Wetzels, A. and Wong, T.E.:
 1533 Jurassic, in: *The Geology of Central Europe Volume 2: Mesozoic and Cenozoic*, edited
 1534 by McCann, T., Geological Society of London, London, 823–922,
 1535 <https://doi.org/10.1144/CEV2P.2>, 2008.
- 1536 Pieńkowski, G., Uchman, A., Ninard, K., and Hesselbo, S. P.: Ichnology, sedimentology,
 1537 and orbital cycles in the hemipelagic Early Jurassic Lurasian Seaway (Pliensbachian,
 1538 Cardigan Bay Basin, UK), *Global Planet. Change*, 207, 103648,
 1539 <https://doi.org/10.1016/j.gloplacha.2021.103648>, 2021
- 1540 Quan, T. M. and Adeboye, O. O.: Interpretation of nitrogen isotope profiles in petroleum
 1541 systems: a review. *Frontiers in Earth Science*, 9, 705691,
 1542 <https://doi.org/10.3389/feart.2021.705691>, 2021.
- 1543 Quesada, S. and Robles, S.: Características y origen del petróleo de Hontomín, Cuenca
 1544 Vasocantábrica (Norte de España), *Geogaceta*, 52, 169-172, ISSN 2173-6545, 2012.
- 1545 Quesada, S., Dorronsoro, C. Robles, S., Chaler, R. and Grimalt, J.O.: Geochemical
 1546 correlation of oil from the Ayoluengo field to Liassic “black shale” units in the

- 1547 southwestern Basque-Cantabrian Basin (northern Spain), *Org. Geochem.*, 27, 25-40,
1548 [https://doi.org/10.1016/S0146-6380\(97\)00045-4](https://doi.org/10.1016/S0146-6380(97)00045-4), 1997.
- 1549 Quesada, S., Robles, S. and Rosales, I.: Depositional architecture and transgressive-
1550 regressive cycles within Liassic backstepping carbonate ramps in the Basque-Cantabrian
1551 Basin, northern Spain, *J. Geol. Soc.*, 162, 531-548, [https://doi.org/10.1144/0016-764903-](https://doi.org/10.1144/0016-764903-041)
1552 041, 2005.
- 1553 Rachold, V. and Brumsack, H. J.: Inorganic geochemistry of Albian sediments from the
1554 Lower Saxony Basin NW Germany: palaeoenvironmental constraints and orbital cycles,
1555 *Palaeogeogr. Palaeoclimatol. Palaeoecol.*, 174(1-3), 121-14,
1556 [https://doi.org/10.1016/S0031-0182\(01\)00290-5](https://doi.org/10.1016/S0031-0182(01)00290-5), 2001.
- 1557 Reuning, L., Reijmer, J. J. and Betzler, C.: Sedimentation cycles and their diagenesis on
1558 the slope of a Miocene carbonate ramp (Bahamas, ODP Leg 166), *Mar. Geol.*, 185(1-2),
1559 121-142, [https://doi.org/10.1016/S0025-3227\(01\)00293-6](https://doi.org/10.1016/S0025-3227(01)00293-6), 2002.
- 1560 Robinson, R.S., Kienast, M., Luiza Albuquerque, A., Altabet, M., Contreras, S., De Pol
1561 Holz, R., Dubois, N., Francois, R., Galbraith, E., Hsu, T.-C., Ivanochko, T., Jaccard, S.,
1562 Kao, S.-J., Kiefer, T., Kienast, S., Lehmann, M., Martinez, P., McCarthy, M., M'obius,
1563 J., Pedersen, T., Quan, T.M., Ryabenko, E., Schmittner, A., Schneider, R., Schneider-
1564 Mor, A., Shigemitsu, M., Sinclair, D., Somes, C., Studer, A., Thunell, R. and Yang, J.-
1565 Y.: A review of nitrogen isotopic alteration in marine sediments, *Paleoceanography*,
1566 27(4), PA4203, doi:10.1029/2012PA002321, 2012.
- 1567 Rosales, I., Quesada, S. and Robles, S.: Primary and diagenetic isotopic signals in fossils
1568 and hemipelagic carbonates: the Lower Jurassic of northern Spain, *Sedimentology*, 48(5),
1569 1149-1169, <https://doi.org/10.1046/j.1365-3091.2001.00412.x>, 2001.
- 1570 Rosales, I., Quesada, S. and Robles, S.: Paleotemperature variations of Early Jurassic
1571 seawater recorded in geochemical trends of belemnites from the Basque-Cantabrian
1572 basin, northern Spain, *Palaeogeogr. Palaeoclimatol. Palaeoecol.*, 203, 253-275,
1573 [https://doi.org/10.1016/S0031-0182\(03\)00686-2](https://doi.org/10.1016/S0031-0182(03)00686-2), 2004.
- 1574 Rosales, I., Quesada, S. and Robles, S.: Geochemical arguments for identifying second-
1575 order sea-level changes in hemipelagic carbonate ramp deposits, *Terra Nova*, 18(4), 233-
1576 240, <https://doi.org/10.1111/j.1365-3121.2006.00684.x>, 2006.
- 1577 Ruhl, M., Hesselbo, S. P., Hinnov, L., Jenkyns, H. C., Xu, W., Riding, J. B., Storm, M.,
1578 Minisini, D., Ullmann, C. V. and Leng, M. J.: Astronomical constraints on the duration
1579 of the Early Jurassic Pliensbachian Stage and global climatic fluctuations, *Earth Planet.*
1580 *Sc. Lett.*, 455, 149-165, <http://dx.doi.org/10.1016/j.epsl.2016.08.038>, 2016.
- 1581 Sames, B., Wagreich, M., Conrad, C. P. and Iqbal, S.: Aquifer-eustasy as the main driver
1582 of short-term sea-level fluctuations during Cretaceous hothouse climate phases, *Geol.*
1583 *Society, London, Sp. Publ.*, 498(1), 9-38, <https://doi.org/10.1144/SP498-2019-105>, 2020.

- 1584 Sarr, A. C., Donnadieu, Y., Laugié, M., Ladant, J. B., Suchéras-Marx, B. and Raison, F.:
1585 Ventilation Changes Drive Orbital-Scale Deoxygenation Trends in the Late Cretaceous
1586 Ocean, *Geophys. Res. Lett.*, 49(19), e2022GL099830,
1587 <https://doi.org/10.1029/2022GL099830>, 2022.
- 1588 Schneider-Mor, A., Alsenz, H., Ashckenazi-Polivoda, S., Illner, P., Abramovich, S.,
1589 Feinstein, S., Almogi-Labin, A., Berner, Z. and Püttmann, W.: Paleooceanographic
1590 reconstruction of the late Cretaceous oil shale of the Negev, Israel: Integration of
1591 geochemical, and stable isotope records of the organic matter, *Palaeogeogr.*
1592 *Palaeoclimatol. Palaeoecol.*, 319, 46-57, <https://doi.org/10.1016/j.palaeo.2012.01.003>,
1593 2012.
- 1594 Sequero, C., Bádenas, B. and Muñoz, A.: Sedimentología y cicloestratigrafía de las
1595 calizas fangosas de plataforma abierta de la Fm. Río Palomar (Pliensbachiense inferior;
1596 Cuenca Ibérica), *Rev. de la Soc. Geol. de Espana*, 30 (1), 71-84, ISSN: 2255-1379, 2017.
- 1597 Silva, R. L., Duarte, L. V., Comas-Rengifo, M. J., Mendonça Filho, J. G. and Azerêdo,
1598 A. C.: Update of the carbon and oxygen isotopic records of the Early–Late Pliensbachian
1599 (Early Jurassic, ~187 Ma): Insights from the organic-rich hemipelagic series of the
1600 Lusitanian Basin (Portugal), *Chem. Geol.*, 283(3-4), 177-184,
1601 <https://doi.org/10.1016/j.chemgeo.2011.01.010>, 2011.
- 1602 Steffen, K., Thomas, R.H., Rignot, E., Cogley, J.G., Dyurgerov, M.B., Raper, S.C.B.,
1603 Huybrechts, P. and Hanna, E.: Cryospheric contributions to sea level rise and variability,
1604 in: *Understanding sea level rise and variability*, edited by Church, J.A., Woodworth, P.L.,
1605 Aarup, T. and Wilson, W.S., Wiley-Blackwell, Chichester, 177–225,
1606 <https://doi.org/10.1002/9781444323276.ch7>, 2010.
- 1607 Storm, M. S., Hesselbo, S. P., Jenkyns, H. C., Ruhl, M., Ullmann, C. V., Xu, W., Leng,
1608 M. J., Riding, J. B. and Gorbanenko, O.: Orbital pacing and secular evolution of the Early
1609 Jurassic carbon cycle, *P. Natl. Acad. Sci. USA*, 117, 3974–3982,
1610 <https://doi.org/10.1073/pnas.1912094117>, 2020.
- 1611 Suan, G., Van De Schootbrugge, B., Adatte, T., Fiebig, J. and Oschmann, W.: Calibrating
1612 the magnitude of the Toarcian carbon cycle perturbation, *Paleoceanography*, 30(5), 495-
1613 509, <https://doi.org/10.1002/2014PA002758>, 2015.
- 1614 Suárez Ruiz, I and Prado, J.G.: Estudio microscópico de la materia orgánica en las
1615 pizarras bituminosas del Lías en el litoral de Cantabria, *Acta Geológica Hispánica*, 21-
1616 22, 585-591, ISSN 1695-6133, 1987.
- 1617 Swart, P. K.: The geochemistry of carbonate diagenesis: The past, present and future,
1618 *Sedimentology*, 62(5), 1233-1304, <https://doi.org/10.1111/sed.12205>, 2015.
- 1619 Swart, P.K., Blättler, C.L., Nakakuni, M., Mackenzie, G.J., Betzler, C., Eberli, G.P.,
1620 Reolid, J., Alonso-Garcia, M., Slagle, A.L., Wright, J.D., Kroon, D., Reijmer, J.J.G., Mee,
1621 A.L.H., Young, J.R., Alvarez-Zarikian, C.A., Bialik, O.M., Guo, J.A. and Haffe, S.:

- 1622 Cyclic anoxia and organic rich carbonate sediments within a drowned carbonate platform
1623 linked to Antarctic ice volume changes: Late Oligocene-early Miocene Maldives, Earth
1624 Planet. Sci. Lett., 521, 1-13, <https://doi.org/10.1016/j.epsl.2019.05.019>; 2019.
- 1625 Torrence, C. and Compo, G.P.: A practical guide to wavelet analysis, Bull. Am. Meteorol.
1626 Soc., 79, 61-78, <https://doi.org/10.1175/1520-0477>, 1998.
- 1627 Tribovillard, N., Algeo, T. J., Lyons, T. and Riboulleau, A.: Trace metals as paleoredox
1628 and paleoproductivity proxies: an update, Chem. geol. 232(1-2), 12-32,
1629 <https://doi.org/10.1016/j.chemgeo.2006.02.012>, 2006.
- 1630 Tucker, M. E., Gallagher, J. and Leng, M. J.: Are beds in shelf carbonates millennial-
1631 scale cycles? An example from the mid-Carboniferous of northern England.... Sediment.
1632 Geol., 214(1-4), 19-34, <https://doi.org/10.1016/j.sedgeo.2008.03.011>, 2009.
- 1633 Tyson, R.V.: The “productivity versus preservation” controversy; cause, flaws, and
1634 resolution, in: Deposition of Organic-Carbon-Rich Sediments: Models, Mechanisms, and
1635 Consequences, edited by: Harris, N.B., Society for Sedimentary Geology (SEPM-SSG),
1636 Special Publication, 82, 17–33, <https://doi.org/10.2110/pec.05.82.0017>, 2005.
- 1637 Ullmann, C. V., Szücs, D., Jiang, M., Hudson, A. J. and Hesselbo, S. P.: Geochemistry
1638 of macrofossil, bulk rock and secondary calcite in the Early Jurassic strata of the Llanbedr
1639 (Mochras Farm) drill core, Cardigan Bay Basin, Wales, UK, J. Geol. Soc., 179(1),
1640 jgs2021-018, <https://doi.org/10.1144/jgs2021-018>, 2022.
- 1641 Val, J., Bádenas, B., Aurell, M. and Rosales, I.: Cyclostratigraphy and chemostratigraphy
1642 of a bioclastic storm-dominated carbonate ramp (late Pliensbachian, Iberian Basin),
1643 Sediment. Geol., 355, 93-113, <https://doi.org/10.1016/j.sedgeo.2017.04.007>, 2017.
- 1644 Van Mooy, B. A., Keil, R. G. and Devol, A. H.: Impact of suboxia on sinking particulate
1645 organic carbon: Enhanced carbon flux and preferential degradation of amino acids via
1646 denitrification, Geochim. Cosmochim. Acta, 66(3), 457-465,
1647 [https://doi.org/10.1016/S0016-7037\(01\)00787-6](https://doi.org/10.1016/S0016-7037(01)00787-6), 2002.
- 1648 Wang, P.: Global monsoon in a geological perspective, Chin. Sci. Bull., 54, 1113–1136,
1649 <https://doi.org/10.1007/s11434-009-0169-4>, 2009.
- 1650 Wendler, J. E. and Wendler, I.: What drove sea-level fluctuations during the mid-
1651 Cretaceous greenhouse climate?, Palaeogeogr. Palaeoclimatol. Palaeoecol., 441, 412-
1652 419, <http://dx.doi.org/10.1016/j.palaeo.2015.08.029>, 2016.
- 1653 Westphal, H.: Limestone–marl alternations as environmental archives and the role of
1654 early diagenesis: a critical review, International Journal of Earth Sciences, 95, 947-961,
1655 DOI 10.1007/s00531-006-0084-8, 2006.
- 1656 Wignall, P. B.: Model for transgressive black shales?, Geology, 19(2), 167-170,
1657 <https://doi.org/10.1130/0091-7613>, 1991.

1658 Woodard, S. C., Thomas, D. J., Hovan, S., Röhl, U. and Westerhold, T.: Evidence for
1659 orbital forcing of dust accumulation during the early Paleogene greenhouse, *Geochem.*
1660 *Geophys.*, 12(2), <https://doi.org/10.1029/2010GC003394>; 2011.

1661 Zhang, R., Jin, Z., Li, M., Gillman, M., Chen, S., Liu, Q., Wei, R. and Shi, J.: Long-term
1662 periodicity of sedimentary basins in response to astronomical forcing: Review and
1663 perspective, *Earth Sci. Rev.*, 104533, <https://doi.org/10.1016/j.earscirev.2023.104533>,
1664 2023.

1665 Zhao, M.Y. and Zheng, Y.F.: Marine carbonate records of terrigenous input into
1666 Paleotethyan seawater: geochemical constraints from Carboniferous limestones,
1667 *Geochim. Cosmochim. Acta*, 141, 508-531, <https://doi.org/10.1016/j.gca.2014.07.001>,
1668 2014.

1669

1670